

# The Influence of Manganese Content on the Stacking-Fault and Austenite/ $\epsilon$ -Martensite Interfacial Energies in Fe-Mn-(Al-Si) Steels Investigated by Experiment and Theory

D.T. Pierce<sup>a</sup>, J.A. Jiménez<sup>b</sup>, J. Bentley<sup>c</sup>, D. Raabe<sup>d</sup>, C. Oskay<sup>e</sup>, J.E. Wittig<sup>e</sup>

<sup>a</sup>Vanderbilt University, PMB 351683, 2301 Vanderbilt Place, Nashville, TN 37232 USA, email: dean.t.pierce@vanderbilt.edu

<sup>b</sup>Centro Nacional de Investigaciones Metalúrgicas (CSIC), Avda. Gregorio del Amo, 8, 28040-Madrid Spain

<sup>c</sup>Microscopy and Microanalytical Sciences, P.O. Box 7103, Oak Ridge, TN 37831-7103 USA

<sup>d</sup>Max-Planck-Institut für Eisenforschung, Max-Planck Str. 1, D-40237 Düsseldorf, Germany

<sup>e</sup>Vanderbilt University, PMB 351683, 2301 Vanderbilt Place, Nashville, TN 37232 USA

## Key Words

TWIP steel, phase stability, partial-dislocation, stacking-fault energy, interface energy

## Abstract

The stacking-fault and interfacial energies of three transformation- and twinning-induced plasticity steels (TRIP/TWIP) (Fe-22/25/28Mn-3Al-3Si wt.%) were determined by experimental and theoretical methods. Analysis of Shockley partial-dislocation configurations in the three alloys using weak-beam dark-field transmission electron microscopy yielded stacking-fault energy (SFE) values of  $15 \pm 3$ ,  $21 \pm 3$  and  $39 \pm 5$   $\text{mJ m}^{-2}$  for alloys with 22, 25 and 28 wt.% Mn, respectively. The experimental SFE includes a coherency strain energy of  $\sim 1\text{-}4$   $\text{mJ m}^{-2}$ , determined with x-ray diffraction, which arises from the contraction in molar volume of the stacking-fault upon the face-centered cubic (FCC) to hexagonal close-packed (HCP) phase transformation. The ideal SFE, computed as the difference between the experimental SFE and the coherency strain energy, is equal to  $14 \pm 3$ ,  $19 \pm 3$  and  $35 \pm 5$   $\text{mJ m}^{-2}$ , respectively. These SFE values were used in conjunction with a thermodynamic model developed in the present work to calculate the free energy difference of the FCC and HCP phases and determine a probable range for the FCC/HCP interfacial energy in the three Fe-Mn-(Al-Si) steels investigated. In addition, the interfacial energies of three Fe-18Mn-0.6C-0/1.5(Al/Si) TWIP and five Fe-

16/18/20/22/25Mn binary alloys were also determined from experimental data in the literature. The interfacial energy in these materials ranged from  $\sim 8\text{-}33 \text{ mJ m}^{-2}$  and is strongly linked to the difference in Gibbs energy of the individual FCC and HCP phases. Accordingly, an empirical description of this parameter is proposed to improve the accuracy of thermodynamic SFE calculations.

## 1. Introduction

High-manganese austenitic transformation- and twinning-induced plasticity (TRIP/TWIP) steels are a superior class of materials that exhibit excellent strain-hardening, strength, ductility and toughness [1-8]. This combination of mechanical properties is attractive for automotive applications requiring high room-temperature formability and weight reduction. These alloys typically include  $\sim 18\text{-}30 \text{ wt.}\%$  Mn and additions of Al, Si, Cr, C and N with microstructures of meta-stable or stable austenite [9-12]. During deformation, the austenite deforms by dislocation glide together with secondary deformation mechanisms including  $\alpha_{\text{bcc}}/\epsilon_{\text{hcp}}$ -martensite formation and/or mechanical twinning [13]. The martensite platelets and mechanical twins act as planar obstacles and reduce the mean free path of dislocation glide. As deformation progresses these strain-induced features increasingly refine the grain structure causing a dynamic Hall-Petch effect [5,14-22]. The result is high-strain hardening, delayed necking and large uniform elongations [1].

The low stacking-fault energy (SFE) of these steels allows for these secondary deformation mechanisms (TRIP/TWIP effect). With decreasing SFE, the plasticity mechanisms change from (i) dislocation glide to (ii) dislocation glide and mechanical twinning to (iii) dislocation glide and  $\gamma_{\text{fcc}} \rightarrow \epsilon_{\text{hcp}}$  martensitic transformations [3, 23-27]. Each deformation mode

results in different mechanical properties. Consequently, designing TRIP/TWIP alloys requires a reliable method of predicting SFE.

Many authors correlate microstructural observations of deformation mechanisms and mechanical properties with thermodynamic calculations of the SFE. The method proposed by Olson and Cohen [28], and adapted by several other authors [3,12,24,26], treats the fault as  $n$  layers of hexagonal close-packed (HCP) phase separated from the face-centered cubic (FCC) matrix by two interfaces. The SFE can be calculated as:

$$\gamma_{\infty} = n\rho(\Delta G_{Chem}^{fcc \rightarrow hcp} + \Delta G_{Mag}^{fcc \rightarrow hcp}) + 2\sigma^{\gamma/\varepsilon} \quad (1)$$

where  $\gamma_{\infty}$  is the ideal SFE ( $\text{mJ m}^{-2}$ ) of the fault (un-bounded by partial dislocations),  $n$  is equal to 2 for an intrinsic stacking-fault,  $\Delta G_{Chem}^{fcc \rightarrow hcp}$  and  $\Delta G_{Mag}^{fcc \rightarrow hcp}$  ( $\text{mJ mol}^{-1}$ ) are the chemical and magnetic contributions to the difference in Gibbs free energy of the FCC and HCP phases. The term  $\Delta G_{Mag}^{fcc \rightarrow hcp}$  arises from antiferromagnetic ordering. With decreasing temperature both the FCC and HCP phases in Fe-Mn based alloys undergo a paramagnetic to antiferromagnetic state change at their respective Néel temperatures [3,4,12,18,24-26]. Antiferromagnetic ordering has a stabilizing influence and lowers the Gibbs free energy of the individual phases. The term  $\sigma^{\gamma/\varepsilon}$  ( $\text{mJ m}^{-2}$ ) is the interfacial energy between the FCC and HCP phase and  $\rho$  is the molar surface density ( $\text{mol m}^{-2}$ ) of  $\{111\}$ , defined in Equation (2):

$$\rho = \frac{4}{\sqrt{3}a_{FCC}^2} \frac{1}{N_A} \quad (2)$$

The term  $N_A$  is Avogadro's number and  $a_{FCC}$  is the lattice parameter of the FCC phase. Allain et al.[24] studied an Fe-22Mn-0.6C wt.% steel and concluded that  $\varepsilon_{hcp}$ -martensite formation occurs for calculated SFEs below  $18 \text{ mJ m}^{-2}$  while mechanical twinning is active from  $12$  to  $35 \text{ mJ m}^{-2}$ .

Thermodynamic SFE calculations by Saeed-Akbari et al. [26] indicate an upper limit of  $20 \text{ mJ m}^{-2}$

<sup>2</sup> for strain-induced  $\epsilon_{\text{hcp}}$ -martensite transformation. Nakano and Jacques [29] calculated SFE values for the Fe-Mn and Fe-Mn-C systems and correlated these with microstructural observations from other investigators, finding strain-induced  $\epsilon_{\text{hcp}}$ -martensitic to occur at SFEs as high as 41 mJ m<sup>-2</sup>. The lack of agreement between SFE value and deformation mechanism in the literature results from different thermodynamic parameters and interfacial energies, with  $\sigma^{\gamma/\epsilon}$  varying from 9 mJ m<sup>-2</sup> (Allain et al.[24]) to 16 mJ m<sup>-2</sup> (Nakano and Jacques [29]). Saeed-Akbari et al. [26] utilized a value of 15 mJ m<sup>-2</sup> but acknowledged the uncertainty of this parameter in Fe-Mn based alloys, citing literature values that ranged from 5 to 27 mJ m<sup>-2</sup>.

The uncertainty of the interfacial parameter in Fe-Mn based systems limits the effectiveness of thermodynamic SFE models. Olson and Cohen [28] proposed to indirectly calculate  $\sigma^{\gamma/\epsilon}$  using experimental SFE values,  $\gamma_{\text{exp}}$ . The term  $\gamma_{\text{exp}}$  includes a coherency strain energy,  $E_{\text{str}}$  (J/mol), arising from the contraction in molar volume of the HCP stacking fault relative to the FCC matrix (note: the same coherency strain energy is not accounted for in thermodynamic SFE values). The strain energy must be subtracted from the experimental SFE value as in Equation (3):

$$\gamma_{\infty} = \gamma_{\text{exp}} - n\rho E_{\text{str}} \quad (3)$$

to yield  $\gamma_{\infty}$ . Combining Equations (1) and (3) gives:

$$\sigma^{\gamma/\epsilon} = \frac{1}{2} \left( \gamma_{\text{exp}} - n\rho (E_{\text{str}} + \Delta G_{\text{Chem}}^{\text{fcc} \rightarrow \text{hcp}} + \Delta G_{\text{Mag}}^{\text{fcc} \rightarrow \text{hcp}}) \right) \quad (4)$$

Cotes et al. [30] used experimental SFE values from measurements of extended dislocation nodes [31,32] to determine room temperature values of  $\sigma^{\gamma/\epsilon}$  ranging from 16 to 26 mJ m<sup>-2</sup>, for binary Fe-Mn alloys. However, by comparison to SFE measurements from Shockley partial-dislocation pairs, measurements from extended dislocation nodes are usually higher and result in greater uncertainty [33,34]. Heat treatments were typically required to form symmetrical nodes

in Fe-Cr-Ni specimens [33]. In that study, the authors found the room temperature node size to vary inversely with prior heat treatment temperature, suggesting the nodes were inhibited from returning to equilibrium configuration after heating. Since the effect was not observed on the separation of partial-dislocation pairs, the authors suggested nodes were more susceptible to solute impedance forces which resulted in higher apparent SFE measurements. However, the general trend in SFE values for different grades of austenitic stainless steel was similar for each method of measurement. In a study by the present authors [34], the formation of nodes in Fe-Mn-Al-Si steels required heat treatments in excess of 650°C and then only resulted in non-isolated and mostly asymmetrical nodes unsuitable for measurement. Therefore, the SFE values reported for binary Fe-Mn alloys [31,32] may overestimate the true values. Consequently, the interfacial energy determined from these SFE values may also be systematically overestimated.

Stacking-fault energy measurements on TRIP/TWIP steels by analysis of partial-dislocation pairs using weak-beam dark-field (WBDF) transmission electron microscopy (TEM) have been reported for Fe-20Mn-1.2C ( $\gamma_{exp}=15 \text{ mJ m}^{-2}$ ) [35], Fe-18Mn-0.6C ( $\gamma_{exp}=13 \pm 3 \text{ mJ m}^{-2}$ ) [10], Fe-18Mn-0.6C-1.5Al ( $\gamma_{exp}=30 \pm 10 \text{ mJ m}^{-2}$ ) [10] and Fe-25Mn-3Al-3Si grades ( $\gamma_{exp}=16 \pm 4 \text{ mJ m}^{-2}$ ) [34]. The following concerns arise from evaluating these studies.

Equilibrium partial-dislocation separations are a balance between the restorative force due to the SFE and the repulsive elastic force of the partial dislocations [36]. Determination of the elastic repulsive force acting on dislocations in anisotropic materials requires the single-crystal elastic constants. The experimental studies rely on bulk elastic properties [10], single-crystal elastic constants from other grades of steel [35] and single-crystal elastic constants from ab-initio simulation [34,37-39]. Recent work by the present authors [40] provides experimental values of single-crystal elastic constants for Fe-Mn-Al-Si and Fe-Mn-C-Al steels necessary for SFE

measurements. As such, the previously reported SFE value of  $16\pm 4$  mJ m<sup>-2</sup> for an Fe-25Mn-3Al-3Si alloy [34] will be updated in the present work by utilizing the more accurate experimental elastic constants. Secondly, in the study on the Fe-18Mn-0.6C-0/1.5Al grades [10], a distinction between the separation of two partial-dislocation images and separation of the cores is not made, which can impact SFE values for small partial-dislocation separations (see sections 3.1 and 4.1). Finally, the effect of Mn content on the SFE cannot be understood from the three studies given the large differences in composition.

The goals of the present study are to:

1. Quantify the influence of Mn content on SFE by applying the elastic constants determined in [40] to Shockley partial-dislocation widths for three Fe-22/25/28Mn-3Al-3Si wt.% alloys.
2. Experimentally determine  $E_{\text{str}}$  and  $\gamma_{\infty}$  for the three Fe-22/25/28Mn-3Al-3Si alloys.
3. Calculate  $\sigma^{\gamma/\epsilon}$  for the three Fe-22/25/28Mn-3Al-3Si alloys and other Fe-Mn based alloys for which experimental SFE data exists in the literature.

In a subsequent paper the observed deformation microstructures and mechanical properties will be reported as a function of Mn content and SFE.

## 2. Materials

Three alloys were induction melted in an argon atmosphere and cast into ingots. The compositions are listed in Table 1. As-cast ingots were thermo-mechanically processed by hot rolling at 1100°C to produce strips of 3 mm thickness and subsequently by cold rolling to 1.5 mm thickness. The resulting sheet was recrystallized at 900°C for 30 min in air, yielding a microstructure with equiaxed grains of  $\sim 21$   $\mu\text{m}$  in diameter for each composition. Oxide layers formed during this treatment were removed by machining. The steels with 25 and 28%Mn were

fully austenitic, while the alloy with 22%Mn contained a small amount of ferrite (<1%) in the recrystallized condition. Sub-sized flat tensile specimens with a 20 mm gauge length and 5 mm width were cut from the sheet in the direction parallel to the rolling direction using electro-discharge machining (EDM).

### 3. Experimental Procedure

Specimens of the 22 25 and 28%Mn alloys were strained in tension at a rate of  $4 \times 10^{-4} \text{ s}^{-1}$  to the yield point (YP) and 1.5% plastic strain for SFE measurements by TEM. Thermal treatments of 650-700°C for 48-70 h were applied to samples strained 1.5% to produce equilibrium dislocation configurations. Additional samples of the 22, 25 and 28%Mn alloys were strained to failure at room temperature, -25 and -100°C, respectively, in order to introduce strain-induced  $\epsilon_{\text{hcp}}$ -martensite for measurement of lattice parameters. The 25 and 28%Mn alloys were deformed at lower temperatures where enough driving force exists to transform sufficient quantities of austenite to  $\epsilon_{\text{hcp}}$ -martensite. Lattice parameters of the FCC and HCP phases were measured by X-ray diffraction (XRD) at room temperature from as-recrystallized (for FCC) and deformed specimens (for HCP).

#### 3.1 Stacking Fault Energy Measurements

Disks 3 mm in diameter were cut from the gauge length of deformed samples using EDM. The 3-mm disks were mechanically polished to 100  $\mu\text{m}$  thickness and then jet electro-polished to electron transparency with a TenuPol-5 using a solution of 70% methanol and 30% nitric acid at -30°C. Partial dislocations were analyzed with a Philips CM20T TEM operating at 200 kV.

Measurements of Shockley partial-dislocation separations were made with a beam direction near the [111] zone on defects in the (111) habit plane using  $\langle -220 \rangle$  type g-vectors.

Bright-field (BF) and WBDF imaging modes were employed with WBDF diffracting conditions set at  $g(3g)$  or  $g(4g)$  with no non-systematic reflections excited. The  $g(3g)$  configuration results in a deviation parameter  $s_g=0.15 \text{ nm}^{-1}$  and  $w= \xi_g s_g=12.4$  where  $\xi_g$  is the extinction distance. The value of  $s_g$  in the  $g(3g)$  configuration is slightly less than the recommended value of  $0.2 \text{ nm}^{-1}$  [41] and results in slightly larger than ideal image widths. For partial-dislocation separations below  $\sim 4 \text{ nm}$ , as in the 28%Mn alloy, the  $g(4g)$  configuration ( $s_g=0.23 \text{ nm}^{-1}$ ,  $w= \xi_g s_g=18.5$ ) was utilized to improve resolution of the partial dislocations. Measurements were made every 5-10 nm along the length of long, straight sections of isolated dislocations in areas not significantly affected by image forces and constrictions. Since the strain fields outside and between partial dislocations are asymmetrical, the intensity peaks are not equidistant from their respective dislocation cores and a correction is applied to determine the actual partial-dislocation spacing,  $d_{\text{actual}}$  [42]. An average  $d_{\text{actual}}$  and standard deviation of the measurements were obtained for each partial-dislocation pair. Inside-outside contrast techniques (reversing the  $g$ -vector) were applied to differentiate partial dislocations from dipoles. The total dislocation character angle,  $\beta$ , was determined from Burgers vector analysis on the partial dislocations in WBDF imaging mode. For Shockley partial dislocations in the  $[111]/(111)$  zone/habit plane configuration,  $|g \bullet b_p|$  (where  $b_p$  is the partial dislocation Burgers vector) values are 1 or 0 and  $|g \bullet b_p| = 1$  for both partials at only one  $g$ -vector. When the latter condition is achieved the total Burgers vector is parallel to the  $g$ -vector and the angle it makes with dislocation line vector is the total dislocation character angle. The habit plane was confirmed by stereographic analysis from BF images of the dislocation taken at three different locations.

### 3.2 X-Ray Diffraction

Measurements of lattice parameters utilized a Bruker AXS D8 diffractometer equipped with a Co X-ray tube, Goebel mirror optics and a LynxEye Linear Position Sensitive Detector for ultra-fast XRD measurements. A current of 30 mA and a voltage of 40 kV were employed as tube settings. Operational conditions were selected to obtain XRD profiles of sufficient quality: namely, optimal counting statistics, narrow peaks and detection of small diffraction peaks of minor phases. The XRD data were collected over a  $2\theta$  range of 30 -120° with a step size of 0.02°.

For the application of the Rietveld refinement, instrument functions were empirically parameterised from the profile shape analysis measured under the same conditions for an AISI Type 316 stainless steel standard prepared by hot isostatic pressing. In this study, version 4.2 of the Rietveld analysis program TOPAS (Bruker AXS) was used for the XRD data refinement. The refinement protocol included the background, zero displacement, scale factors, peak width, unit cell parameters and texture parameters. The room-temperature structures used in the refinement were ferrite, austenite and  $\epsilon_{\text{hcp}}$ -iron. The quality and reliability of the Rietveld analysis was quantified by the corresponding figures of merit: the weighted summation of the residual of the least-squares fit,  $R_{\text{wp}}$ , the statistically expected least-squares fit,  $R_{\text{exp}}$ , the profile residual,  $R_{\text{p}}$ , and the goodness of fit (sometimes referred to as chi-squared), GoF. Since  $\text{GoF} = R_{\text{wp}} / R_{\text{exp}}$ , a  $\text{GoF} = 1.0$  means a perfect fitting.

## **4. Results and Discussion**

### **4.1 Stacking-Fault Energy Measurements**

Additions of Mn from 22 to 28 wt.% increase the SFE and reduce the partial-dislocation separations. Partial-dislocation core separations in the 22%Mn alloy ranged from 6 to 13 nm depending on character angle. Figure 1a displays a WBDF image of a partial-dislocation pair

with a character angle of  $39^\circ$  in a specimen deformed to the YP. The average actual partial-dislocation core separation is  $9.3 \pm 1.1$  nm, in which the uncertainty is one standard deviation of all measurements along the length of the dislocation (note: measurements were taken every 5-10 nm along the length of dislocations but most are removed from the Figures for clarity). The BF image in Figure 1b of the same dislocation illustrates the increased resolution of the WBDF technique. In Figure 1c, a dislocation pair in a 22%Mn specimen deformed to the YP with a smaller character angle of  $26^\circ$  exhibits an average core separation of  $6.6 \pm 0.5$  nm. Due to a low SFE, partial-dislocation separations in the 22%Mn alloy displayed greater variations and susceptibility to image forces, as evidenced by partial dislocations in specimens deformed to the YP in Figure 2. The width of the partials in Figure 2a fluctuates dramatically at the foil surfaces, where the partials are constricted at one intersection while showing a large separation distance at the other. In Figure 2b, a partial-dislocation pair in the (111) habit plane normal to the [111] beam, imaged with a  $-220$  g-vector, is interacting with a stacking fault on (-111). The partial dislocations in (111) experience a contraction in their separation at the intersection with the partial dislocation on the inclined plane. In an image of the same defects with a  $02-2$  g-vector (Figure 2c), one of the partials on (111) and SF on (-111) become invisible ( $|\mathbf{g} \cdot \mathbf{b}_p| = 0$ ). This study avoided partial dislocations such as those in Figure 2 for quantitative measurements.

The separation of partials in the 25%Mn alloy fell between 4 and 7 nm, with Figure 3 showing a partial-dislocation pair with average actual spacing of  $4.9 \pm 0.5$  nm and a total character angle of  $22^\circ$ . The present authors reported additional measurements of dislocations from this alloy in [34].

Partial-dislocation separations in the 28%Mn alloy ranged from 2.6 to 4.3 nm. Imaging with  $g(4g)$  diffracting conditions decreased image-widths and reduced the discrepancy between

observed and actual partial-dislocation separations. In figure 4a, a partial-dislocation pair with kinks or jogs along its length and a character angle of 40° exhibits an average actual spacing of 3.3 nm on uniform sections. In Figure 4b a partial-dislocation pair with a character angle of 15° displays an average actual spacing of 2.5 nm. At small spacing the intensity of the partial-dislocation image located between the partial-dislocation cores becomes significantly weaker due to fewer atomic planes oriented for scattering, as clearly shown in Figure 4b.

The character of stacking faults (intrinsic vs. extrinsic) in the present alloys, as determined by typical diffraction contrast methods (e.g., Williams and Carter [43] and Edington [44]), is intrinsic. Figures 5a, b and c display three dark-field TEM micrographs of stacking faults corresponding to the 22, 25 and 28%Mn alloys respectively. Of ~10 faults investigated for each alloy, all were intrinsic.

Figure 6 displays the average spacing of partial-dislocation pairs in the three alloys. Theoretical partial-dislocation spacing curves based on Equation (5), formulated by Aerts et al. [45], are fit to the experimental data to determine the SFE. The relationship is an excellent approximation of anisotropic theory, as shown by Teutonico [46], and avoids the significant complexity of pure anisotropic dislocation theory [47-49], in which solutions are available only for specific dislocation configurations.

$$d_{actual} = \frac{\mu_{eff} b_p^2}{8\pi\gamma_{exp}} \frac{2-\nu_{eff}}{1-\nu_{eff}} \left( 1 - \frac{2\nu_{eff}\cos 2\beta}{2-\nu_{eff}} \right) \quad (5)$$

The term  $b_p$  is the  $a_0/6\langle 112 \rangle$  partial-dislocation Burgers vector, determined by XRD of recrystallized Fe-22/25/28Mn-3Al-3Si specimens to be 0.1476, 0.1477 and 0.1479 nm, respectively. The total dislocation character angle is  $\beta$  and effective shear modulus,  $\mu_{eff}$ , for dislocations in  $\{111\}$  is a function of the single-crystal elastic stiffness constants  $C_{11}$ ,  $C_{12}$  and  $C_{44}$ , and defined by equation (6):

$$\mu_{eff} = \left( C_{44} \frac{(C_{11}-C_{12})}{2} \right)^{0.5} \quad (6)$$

Equations (7) and (8) denote the relationship between the effective Poisson ratio,  $\nu_{eff}$ , and the single-crystal elastic constants.

$$\frac{1}{1-\nu_{eff}} = \frac{1}{3\mu_{eff}} (C + C_{12}) \left[ \frac{C_{44}(C-C_{12})}{C_{11}(C+C_{12}+2C_{44})} \right]^{0.5} \left( 1 + 2 \frac{C_{11}}{C} \right) \quad (7)$$

$$C = \left[ \frac{1}{2} C_{11} (C_{11} + C_{12} + 2C_{44}) \right]^{0.5} \quad (8)$$

For the 22, 25 and 28%Mn alloys, respectively,  $\mu_{eff}=67\pm4$ ,  $66\pm4$ ,  $66\pm4$  GPa and  $\nu_{eff}=0.30$ ,  $0.31$  and  $0.31$ . The terms  $\mu_{eff}$  and  $\nu_{eff}$  account for anisotropic elasticity in  $\{111\}$  and are calculated from equations (6-8) using single-crystal elastic constants determined by the present authors [40]. The experimental SFEs for the 22, 25 and 28%Mn alloys are  $15\pm3$ ,  $21\pm3$  and  $40\pm5$  mJ m<sup>-2</sup>, respectively. The large increase in SFE energy above 25 wt.% Mn is consistent with experimental observations that show a sharp reduction in the  $\epsilon$ -martensite start temperature for additions of Mn above 25 wt.% in binary Fe-Mn alloys [29,30]. The uncertainty of the SFE is primarily due to the scatter of average  $d_{actual}$  values between different dislocations (data points in Figure 6) and uncertainties of  $\nu_{eff}$  and  $\mu_{eff}$ . The first two sources of uncertainty are accounted for by fitting upper and lower bounds (SFE curves) that encompass the majority of the data points for a given composition as shown in Figure 6. The uncertainty from these two sources was determined to be  $\pm 20.0$ ,  $\pm 14.3$  and  $\pm 12.5\%$  of the SFE for the 22, 25 and 28%Mn alloys, respectively. The uncertainty of  $\mu_{eff}$  is  $\pm 6.03\%$ . The final uncertainty of the SFE for the 22, 25 and 28%Mn alloys was obtained from the root sum square of the two calculated values and is  $\pm 20.9$  (e.g.,  $(20.0^2 + 6.03^2)^{\frac{1}{2}}$ ),  $\pm 15.5$  and  $\pm 13.9\%$  or  $\pm 3$ ,  $\pm 3$  and  $\pm 5$  mJ m<sup>-2</sup> (rounded to one significant figure). Volosevich et al. [31] reported SFE values of  $\sim 15$  and  $27.5$  mJ m<sup>-2</sup> for Fe-22/25Mn wt.% alloys, respectively, by TEM observation of extended nodes. These values likely

overestimate the SFE, since the combined effect of adding 3 wt.% Al and Si would raise the SFE, yet the SFE values of the Fe-22/25Mn-3Al-3Si steels are equal or less. If isotropic elasticity is applied to the measurements on the 22%Mn alloy, by replacing the effective elastic constants in Equation (5) with a polycrystalline shear modulus (72 GPa) and Poisson ratio (0.24) [40], the SFE is  $16 \pm 4 \text{ mJ m}^{-2}$  (dashed lines in Figure 6). The SFE determined with isotropic elastic constants overestimates the anisotropic value by  $\sim 7\%$  and results in a poorer data fit, producing a larger uncertainty of  $\pm 4 \text{ mJ m}^{-2}$ . The overestimation of the SFE results from the use of the larger isotropic shear modulus and the poorer data fit stems from the large difference between the isotropic and effective values of the Poisson ratio. The elastic anisotropy ratio ( $2C_{44}/(C_{11}-C_{12})$ ) of the present materials is  $\sim 2.2$  [40]. For FCC materials,  $\mu_{\text{eff}}$  and  $\nu_{\text{eff}}$  will become increasingly smaller and larger, respectively, relative to the polycrystalline values, as the elastic anisotropy ratio increases [46].

In the above analysis, the partial dislocation cores are treated as purely elastic defects, i.e. as singular Volterra type dislocations with a core width of zero. However, the core width of dislocations may not be zero and, at small partial-dislocation separations, such as those observed in the 28%Mn alloy, core effects can influence SFE measurements as shown by Cockayne and Vitek [50]. The dislocation core thickness can influence the force acting between two partial dislocations and thus, their separation. The partial-dislocation separation obtained from a Peierls type core model,  $d_{\text{Peierls}}$ , which accounts for core width, is related to the partial-dislocation separation of Equation (5),  $d_{\text{actual}}$ , by Equation (9) [50]:

$$d_{\text{Peierls}} = \frac{1}{2} \left( d_{\text{actual}} + \sqrt{d_{\text{actual}}^2 - 4\zeta^2} \right) \quad (9)$$

In this model, as core width increases, the repulsive force acting between the two partial dislocations decreases. Since the core width,  $\zeta$ , is unknown, a reasonable approximation is twice

the lattice parameter (0.724 nm), as employed by Cockayne and Vitek [50]. Applying this model to the partial-dislocation separation measurements of the 28%Mn alloy yields a SFE of 37.5 mJ m<sup>-2</sup> as depicted in Figure 6 (dash-dot line), which is slightly smaller than 40 mJ m<sup>-2</sup> obtained assuming singular cores. The fit of Equation (9) to the partial dislocation separation measurements of the 28%Mn alloy becomes increasingly worse as the core thickness is increased above 0.724 nm. Therefore, the true value of the partial-dislocation core width for the 28%Mn alloy is likely between 0 and 0.724 nm. As such, the SFE of the 28%Mn alloy is taken as the average of the two SFE values, 38.8 ±5 mJ m<sup>-2</sup>. Since the partial-dislocation separations of the 22 and 25%Mn alloys are substantially larger, assuming a core width of 0.724 nm in these alloys produced no significant change in the SFE. Cockayne and Vitek [50] also suggested that partial-dislocation core widths greater than twice the lattice constant may lead to a less well defined image peak and an additional narrow image peak under certain circumstances [50]. No such features observed in the WBDF images for each alloy could be attributed to these effects giving further confidence that the partial dislocation core thickness is below 0.724 nm.

#### 4.2 Coherency Strain Energy Contribution

The FCC matrix and  $\epsilon_{\text{hcp}}$ -martensite have the  $(111)_{\gamma}|| (0001)_{\epsilon} / [1-10]_{\gamma} || [1-210]_{\epsilon}$  orientation relationship. However, the  $\epsilon_{\text{hcp}}$ -martensite phase displays a slightly smaller molar volume than the austenite phase. Brooks et al. [51] showed the local close packed plane (CPP) spacing of single stacking faults contracts ~2% relative to the CPP spacing of the austenitic matrix in Fe–Cr–Ni steels, and thus that stacking faults are  $\epsilon_{\text{hcp}}$ -martensite embryos or nuclei. Marinelli et al. [52,53] observed decreases in the molar volume of the  $\epsilon_{\text{hcp}}$ -martensite structure of ~2% relative to austenite in binary Fe-Mn alloys. The propensity to contract is resisted by the matrix (i.e., austenite phase), which results in the deformation of both austenite matrix and the martensite

phase. This *coherency* strain increases the energy of the stacking fault complex. It is desirable to remove the coherency strain-induced energy contribution from the SFE of experimental measurements so that comparison to theoretical SFE values is applicable. The molar volume of the FCC and HCP phases are defined in equations (10) and (11) as:

$$V_{m,FCC} = \frac{a_{FCC}^3}{4} N_A \quad (10)$$

and

$$V_{m,HCP} = \frac{\sqrt{3}}{4} a_{HCP}^2 c_{HCP} N_A \quad (11)$$

, respectively, where  $a_{FCC}$ ,  $a_{HCP}$  and  $c_{HCP}$  are the lattice constants of the FCC and HCP phases.

The volumetric strain ( $VS$ ) due to volume change from FCC to HCP phase is defined as:

$$VS = \frac{V_{m,HCP} - V_{m,FCC}}{V_{m,FCC}} \quad (12)$$

The strain ( $\varepsilon_{33}$ ) corresponding to the contraction normal to the close packed planes of the HCP structure relative to the FCC matrix is defined as:

$$\varepsilon_{33} = (c_{HCP} - c_{FCC})/c_{FCC} \quad (13)$$

The terms  $c_{FCC}$  and  $c_{HCP}$  are twice the CPP spacing in the FCC and HCP structures, respectively.

The strain terms  $\varepsilon_{11}$  and  $\varepsilon_{22}$  correspond to the contraction along  $\langle 1-210 \rangle$  relative to  $\langle 1-10 \rangle$  (close packed directions) and  $\langle 1-100 \rangle$  relative to  $\langle 11-2 \rangle$ , respectively, and are calculated similarly to  $\varepsilon_{33}$  (Equation (13)) as a function of the lattice parameters. Several authors have investigated the energy contribution of the coherency strain,  $E_{str}$ , on SFE measurements (e.g., [28,30,54]). Olson and Cohen [28] considered the strain energy term to be the sum of a dilatation energy,  $E_{dil}$ , and a shear energy,  $E_{sh}$ :

$$E_{str} = E_{dil} + E_{sh} \quad (14)$$

where

$$E_{dil} = \frac{2(1+\nu)}{9(1-\nu)} \mu V_{m,FCC} (MVS)^2 \quad (15)$$

and

$$E_{sh} = \eta V_{m,FCC} 2\mu \left\{ \frac{1}{6} [(\varepsilon_{11} - \varepsilon_{22})^2 + (\varepsilon_{22} - \varepsilon_{33})^2 + (\varepsilon_{33} - \varepsilon_{22})^2] + \varepsilon_{12}^2 + \varepsilon_{23}^2 + \varepsilon_{13}^2 \right\} \quad (16)$$

The terms  $\nu$  and  $\mu$  represent the austenite phase polycrystalline Poisson's ratio and shear modulus, respectively [40]; and  $\eta$  is the accommodation factor further described below. Equations (15) and (16) are based on the work of Eshelby [55] for determining the strain energy of an inclusion which undergoes a shape change within an infinite matrix. The Olson and Cohen model does not consider the interaction energy between the contracted stacking fault and the partial dislocations. However, Müllner and Ferreira [54] modeled the strain field generated by two parallel partial dislocations and a contracted stacking-fault using Somigliana dislocations to compute the total energy including the interaction components. The interaction energy components involving the two Shockley partials were found to be small or vanishing compared to other components of the coherency strain energy. The Müllner and Ferreira model assumes that the coherency strain is volume preserving (i.e.,  $VS=0$ ), which contrasts with our experimental measurements. Therefore, the method of Olson and Cohen has been used to estimate the coherency strain energy in this study.

The orientation of the principal strain axes  $\varepsilon_{11}$ ,  $\varepsilon_{22}$  and  $\varepsilon_{33}$  are assumed to remain unchanged by the transformation resulting in values of 0 for shear strains  $\varepsilon_{12}$ ,  $\varepsilon_{23}$  and  $\varepsilon_{13}$ . The accommodation factor ( $\eta$ ) is the ratio between the total energy per unit inclusion (i.e., martensite phase) volume embedded in the austenite phase to the energy per unit inclusion volume embedded in a hypothetical rigid matrix [28,55]. For pure dilatation  $\eta$  is constant regardless of particle shape and is built in to Equation (15). For shear strain,  $\eta$  may vary from 0 to 1 depending

on particle shape and the strain state [55]. Following [28,30],  $\eta$  for a spherical inclusion, which is independent of strain state, is employed:

$$\eta = \frac{7-5\nu}{15(1-\nu)} \quad (17)$$

Table 2 provides the lattice parameters of the FCC and  $\epsilon_{\text{hcp}}$ -martensite phases obtained from the Rietveld refinement of XRD patterns from recrystallized specimens (for FCC) and those displayed in Figure 7 from specimens deformed to failure (for HCP), with uncertainty representing equipment error. The XRD patterns in Figures 7a, b and c are from the 22, 25 and 28%Mn samples after deformation to failure at RT, -25°C and -100°C, respectively. The presence of strain-induced  $\epsilon$ -martensite is confirmed for each condition, while the formation of strain-induced  $\alpha$ -martensite is noted in the 22 and 25%Mn alloys.

A slight increase in the lattice parameters of the FCC phase with Mn content is observed while no trend in the HCP lattice parameters can be deduced over the current range of Mn. Utilizing the lattice parameters from Table 2 in conjunction with the method reported by Olson and Cohen [28] yields  $\epsilon_{11}$ ,  $\epsilon_{22}$ ,  $\epsilon_{33}$ ,  $VS$ ,  $E_{dil}$ ,  $E_{sh}$  and  $2\rho E_{str}$  as shown in Table 3. The uncertainties, calculated using a root sum square approach, are ~25% for  $\epsilon_{11}$ ,  $\epsilon_{22}$  and  $\epsilon_{33}$  and ~43% for  $VS$ . The uncertainties are ~62 and 79% for  $E_{dil}$  and  $E_{sh}$ . The value of  $E_{sh}$  is small compared to  $E_{dil}$  for the Fe-22/25/28Mn-3Al-3Si alloys and consequently, the uncertainty of  $2\rho E_{str}$  is also ~62%. The values of VS ranged from -0.011 to -0.018 (-1.1 to -1.8%). Notwithstanding a substantial uncertainty in the calculation of the strain components, the experimental data suggests that contraction increases with Mn content. This is in line with the previous studies conducted on binary Fe-Mn steels [52,53]. The value of  $(E_{sh} + E_{dia})$  calculated by Olson and Cohen is 41.9 mJ mol<sup>-1</sup> for an Fe-Cr-Ni steel and similar to the values calculated here (see Table 3). In addition, Müllner and Ferreira [54] calculated a value of 4.3 mJ m<sup>-2</sup> for  $2\rho E_{str}$  for a type 316

austenitic steel which is similar to the values calculated in the present work of  $1.4 \pm 0.87$ ,  $2.3 \pm 1.4$  and  $3.6 \pm 2.2$  mJ m<sup>-2</sup> for the Fe-22/25/28Mn-3Al-3Si alloys, respectively.

Figure 9 shows the experimental effective ( $\gamma_{\text{exp}}$ ) and ideal ( $\gamma_{\infty}$ ) SFE values. The ideal values,  $\gamma_{\infty}$ , represent the experimental values less the term  $n\rho E_{\text{str}}$ . The dependence of  $\gamma_{\infty}$  on Mn content for Fe-22-28Mn-3Al-3Si wt.% alloys is approximated by Equation (18):

$$\gamma_{\infty} = 0.675X^2 - 29.453X + 334.6 \quad (\text{mJ m}^{-2}) \quad (18)$$

where X is the Mn content in wt.%. The second order polynomial approximation to the SFE displays a minimum at 21.8 wt.% and increases with further additions of Mn. Experimentally, Volosevich et al. [31] observed a similar SFE minimum at 22 wt.% Mn in binary Fe-Mn alloys, followed by a sharp increase in SFE with additions of Mn.

### 4.3 Thermodynamic Modeling

To determine the interfacial energy from Equation 4, a new thermodynamic model was developed to calculate  $\Delta G_{\text{Chem}}^{fcc \rightarrow hcp}$  and  $\Delta G_{\text{Mag}}^{fcc \rightarrow hcp}$  for the present Fe-Mn-Al-Si-C system. Existing thermodynamic models [3,12,25,26,29] for Fe-Mn based steels were evaluated and deemed unsuitable for the present study for several reasons. The models of Saeed-Akbari et al. [26], Mosecker and Saeed-Akbari [12] and Nakano and Jacques [29] address the Fe-Mn-Al-C, Fe-Cr-Mn-N and Fe-Mn-C systems, respectively, but do not attempt to specifically address the influence of Si. The model of Dumay et al. [25] shows that additions of Si up to ~4 wt.% increase the SFE while further additions decrease the SFE of an Fe-22Mn-0.6C steel. The model of Curtze et al. [3] utilizes the same thermodynamic parameters for both pure Si and its interaction with Fe as that of Dumay et al. [25]. A thermodynamic model by Tian and Zhang [60] also predicts an increase in SFE for Fe-31Mn-xSi-0.77C (x=at.%) alloys for Si additions up to 10.2 at%. However, experimental studies on Fe-18Mn-0.6C-0/1.5Si [11] wt.% and Fe-31Mn-

xSi-0.77C at.% [61] alloys report decreases in the SFE with additions of Si, contradicting the thermodynamic models. Also, the more recent thermodynamic models of Nakano and Jacques [29] and Mosecker and Saeed-Akbari [12] show that the treatment of interstitial elements like C is enhanced by the use of a sub-lattice type thermodynamic model. Finally, improved thermodynamic parameters for the Mn-C and Fe-Mn-C systems have recently been published by Djurovic et al [62,63]. For the new model, the FCC and HCP phases were treated as randomly mixed substitutional solutions with two sublattices: substitutional and interstitial [12, 29]:



with  $\lambda$  equal to 1 for FCC and 0.5 for HCP, assuming that interstitial elements do not occupy neighboring octahedral sites in the HCP structure [29, 64]. The term “Va” stands for vacancy.

The terms  $G_m^{hcp}$  and  $G_m^{fcc}$  are the molar Gibbs free energy of the individual phases,  $\Phi$  (FCC or HCP) [12, 29]:

$$G_m^\phi = y_{Fe}^\phi y_C^\phi {}^0G_{Fe:C}^\phi + y_{Fe}^\phi y_{Va}^\phi {}^0G_{Fe:Va}^\phi + y_{Mn}^\phi y_C^\phi {}^0G_{Mn:C}^\phi + y_{Mn}^\phi y_{Va}^\phi {}^0G_{Mn:Va}^\phi + y_{Al}^\phi \left( \frac{y_{Va}^{FCC} + y_{Va}^{HCP}}{2} \right) {}^0G_{Al:Va}^\phi + y_{Si}^\phi \left( \frac{y_{Va}^{FCC} + y_{Va}^{HCP}}{2} \right) {}^0G_{Si:Va}^\phi + RT \left( y_{Fe}^\phi \ln y_{Fe}^\phi + y_{Mn}^\phi \ln y_{Mn}^\phi + \lambda y_C^\phi \ln y_C^\phi + \lambda y_{Va}^\phi \ln y_{Va}^\phi + y_{Al}^\phi \ln y_{Al}^\phi + y_{Si}^\phi \ln y_{Si}^\phi \right) + ex G_m^\phi \quad (20)$$

In Equation (20), R is the gas constant and T is the temperature in K. The site fractions of the individual elements,  $y_i$ , in the substitutional lattice are calculated as:

$$y_i = \frac{x_i}{(1-x_C)} \quad (21)$$

and for C in the interstitial lattice as:

$$y_C = \frac{x_C}{\lambda(1-x_C)} \quad (22)$$

where  $x$  is the mole fraction of each element. Equations (23) defines the correlation between the individual site fractions:

$$y_{Fe} + y_{Mn} + y_{Al} + y_{Si} = y_C + y_{Va} = 1 \quad (23)$$

The thermodynamic parameters  $G_{i:Va}^\phi$  and  $G_{i:C}^\phi$  in Equation (20) are listed in Table 4. They represent the Gibbs energy of substitutional element  $i$  in phase  $\Phi$  when all available interstitial sites are vacant (Va) or occupied by C, respectively. The terms  ${}^0G_{Al:C}^\phi$  and  ${}^0G_{Si:C}^\phi$  were not included in Equation (20) due to a lack of data for the HCP phase. In addition, average vacancy site fractions,  $\left(\frac{y_{Va}^{HCP} + y_{Va}^{FCC}}{2}\right)$ , were used for Si and Al and resulted in significantly better agreement with experimental results for steels with Si and C. The combined term  $\Delta {}^0G_{Si:Va}^{HCP \rightarrow FCC}$  replaces  ${}^0G_{Si:Va}^{HCP}$ ,  ${}^0G_{Si:Va}^{FCC}$  and  $RTy_{Si}^\phi \ln y_{Si}^\phi$  in the calculation of  $\Delta G_{Chem}^{fcc \rightarrow hcp}$ . The excess free energy is described as [29]:

$$\begin{aligned} {}^{ex}G_m^\phi = & y_{Fe}^\phi y_{Mn}^\phi y_C^\phi L_{Fe,Mn:C}^\phi + y_{Fe}^\phi y_{Mn}^\phi y_{Va}^\phi L_{Fe,Mn:Va}^\phi + y_{Fe}^\phi y_C^\phi y_{Va}^\phi L_{Fe:C,Va}^\phi + y_{Mn}^\phi y_C^\phi y_{Va}^\phi L_{Mn:C,Va}^\phi + \\ & y_{Fe}^\phi y_{Al}^\phi \left(\frac{y_{Va}^{FCC} + y_{Va}^{HCP}}{2}\right) L_{Fe,Al:Va}^\phi + y_{Mn}^\phi y_{Al}^\phi \left(\frac{y_{Va}^{FCC} + y_{Va}^{HCP}}{2}\right) L_{Mn,Al:Va}^\phi + y_{Fe}^\phi y_{Si}^\phi \left(\frac{y_{Va}^{FCC} + y_{Va}^{HCP}}{2}\right) L_{Fe,Si:Va}^\phi + \\ & y_{Mn}^\phi y_{Si}^\phi \left(\frac{y_{Va}^{FCC} + y_{Va}^{HCP}}{2}\right) L_{Mn,Si:Va}^\phi \end{aligned} \quad (24)$$

where  $L_{i,j:C,Va}^\phi$  is the interaction parameter for the elements in phase  $\Phi$ , listed in Table 4.

Parameters describing the interaction of Al and Si with C were not available for the HCP phase.

Average vacancy site fractions were used for  $L_{Fe,Al:Va}^\phi$ ,  $L_{Mn,Al:Va}^\phi$ ,  $L_{Fe,Si:Va}^\phi$  and  $L_{Mn,Si:Va}^\phi$  to

improve agreement with experimental SFE measurements of steels with interstitial C. For

aluminium, the combined term  $\Delta L_{Fe,Al:Va}^{HCP \rightarrow FCC}$  replaces  $L_{Fe,Al:Va}^\phi$  in Equation (24) for the calculation

of  $\Delta G_{Chem}^{fcc \rightarrow hcp}$ .

The magnetic contribution to the Gibbs energy of a phase is described by Hillert and Jarls [74] modification to the model proposed by Inden [75]:

$$G_{Mag}^\phi = RT \ln(\beta^\phi + 1) f^\phi(\tau^\phi) \quad (25)$$

The term  $\beta^\Phi$  is the magnetic moment of phase  $\Phi$  divided by the Bohr magneton  $\mu_b$  and given by Equations (26) and (27) [25].

$$\beta^{FCC} = 0.7x_{Fe} + 0.62x_{Mn} - 0.64x_{Fe}x_{Mn} - 4x_C \quad (26)$$

$$\beta^{HCP} = 0.62x_{Mn} - 4x_C \quad (27)$$

The term  $f^\Phi(\tau^\Phi)$  is a function of the scaled Néel temperature  $\tau^\Phi = T/T_{Neel}^\Phi$ , found elsewhere in the literature [3,26,65,74,75]. The Néel temperature for the FCC phase of Fe-Mn-Al-Si steels is described by King and Peters [58] as:

$$T_{Neel}^{FCC} = 199.5 + 6.0X_{Mn} - 10.4X_{Al} - 13X_{Si} \quad (K) \quad (28)$$

where X is the wt.% of the individual elements and for the HCP phase as [59]:

$$T_{Neel}^{HCP} = 580x_{Mn} \quad (K) \quad (29)$$

In Equation (29),  $x_{Mn}$  is the molar fraction of Mn. If the lattice parameters of the materials are unknown, they may be estimated as a function of composition and temperature from equations listed in reference [26].

At room temperature (25°C), the model predicts  $(\Delta G_{Chem}^{fcc \rightarrow hcp} + \Delta G_{Mag}^{fcc \rightarrow hcp})$  to be -88 J mol<sup>-1</sup> for the alloy with 22%Mn. This is a reasonable value considering thermal  $\epsilon_{hcp}$ -martensite is not present yet mechanical  $\epsilon_{hcp}$ -martensite forms upon deformation. Thermal  $\epsilon_{hcp}$ -martensite typically occurs when  $(\Delta G_{Chem}^{fcc \rightarrow hcp} + \Delta G_{Mag}^{fcc \rightarrow hcp}) < -100$  J mol<sup>-1</sup> [25] while mechanical  $\epsilon_{hcp}$ -martensite is generally observed in Fe-Mn based alloys where  $(\Delta G_{Chem}^{fcc \rightarrow hcp} + \Delta G_{Mag}^{fcc \rightarrow hcp})$  is negative [12]. Thermal  $\epsilon_{hcp}$ -martensite forms in a similar alloy (Fe-20Mn-3Al-3Si wt.%) with slightly less Mn content [23]. At 25%Mn, the term  $(\Delta G_{Chem}^{fcc \rightarrow hcp} + \Delta G_{Mag}^{fcc \rightarrow hcp})$  is positive and equal to 31 J mol<sup>-1</sup> and the dominant secondary deformation mechanism is mechanical twinning [23]. These results are consistent with previous observations that Fe-Mn based alloys with

negative or positive values of  $(\Delta G_{Chem}^{fcc \rightarrow hcp} + \Delta G_{Mag}^{fcc \rightarrow hcp})$  tend to exhibit strain-induced  $\epsilon_{hcp}$ -martensite or mechanical twinning, respectively [12].

Figure 8 displays the trends in  $2\rho\Delta G_{Chem}^{fcc \rightarrow hcp}$ ,  $2\rho\Delta G_{Mag}^{fcc \rightarrow hcp}$  and  $\sigma^{Y/\epsilon}$  as a function of Mn content. The chemical contribution,  $2\rho\Delta G_{Chem}^{fcc \rightarrow hcp}$ , increases with increasing Mn content from 22 to 28 wt.%, exhibiting a slight concave up trend due to the stabilizing effect that Mn has on the FCC phase relative to the HCP. For the compositions analyzed, the increase in  $2\rho\Delta G_{Chem}^{fcc \rightarrow hcp}$  is  $\sim 3 \text{ mJ m}^{-2}$  per wt.% Mn, agreeing well with the experimentally observed SFE between 22 and 25 wt.% Mn. The calculation of  $2\rho\Delta G_{Chem}^{fcc \rightarrow hcp}$  was also performed using the thermodynamic parameter  $L_{Fe,Mn:Va}^{HCP}$  proposed by Djurovic et al. [63] (dashed line in Figure 8). However, the calculated value of  $2\rho\Delta G_{Chem}^{fcc \rightarrow hcp}$  using the  $L_{Fe,Mn:Va}^{HCP}$  proposed by Nakano and Jacques [29] more closely agreed with the present experimental SFE measurements.

The HCP phase in each alloy is in the paramagnetic state at RT (the Néel temperatures are 123, 137 and 153K for the 22, 25 and 28% Mn alloys, respectively, based on Equation (29)). Consequently, the influence of antiferromagnetic ordering on the HCP phase is insignificant at RT and  $G_{Mag}^{HCP} \approx 0 \text{ J mol}^{-1}$  for the three alloys. The FCC phase of the alloys with 22 and 25% Mn are paramagnetic at RT (Néel temperatures are 267 and 282K, respectively) while the FCC phase of the 28%Mn has a Néel temperature of  $\sim 298\text{K}$  based on Equation (28). The calculated values of  $G_{Mag}^{FCC}$  are -26, -34 and -45  $\text{J mol}^{-1}$  for the 22, 25 and 28%Mn alloys, respectively. Therefore,  $2\rho\Delta G_{Mag}^{fcc \rightarrow hcp}$  is small and increases from 1.5 to 2.6  $\text{mJ m}^{-2}$  with increasing Mn content (see Figure 8). For the present range of Mn content, the term  $(2\rho\Delta G_{Chem}^{fcc \rightarrow hcp} + 2\rho\Delta G_{Mag}^{fcc \rightarrow hcp})$  increases by 3.2  $\text{mJ m}^{-2}$  per wt.% Mn, a slight increase compared to the rise due only to the chemical contribution. As Fe-Mn based alloys are cooled below  $T_{Neel}^{FCC}$ , the influence of

antiferromagnetic ordering on properties such as electrical resistance and stiffness are gradual [57,58,76]. Accordingly, increasing  $T_{Neel}^{FCC}$  through room temperature by additions of Mn should produce only a gradual stabilization of the FCC phase due to magnetic ordering as the model currently predicts. However,  $\Delta G_{Mag}^{fcc \rightarrow hcp}$  becomes large for alloys that are cooled significantly below  $T_{Neel}^{FCC}$  [3] and partially counteracts the reduction in  $\Delta G_{Chem}^{fcc \rightarrow hcp}$  with cooling. This explains why low deformation temperatures (-25 and -100°C) are required to form sufficient quantities of  $\epsilon_{hcp}$ -martensite in the 25 and 28%Mn alloys. The sensitivity of the SFE to temperature becomes less below  $T_{Neel}^{FCC}$  [29] due to the competing nature of  $\Delta G_{Chem}^{fcc \rightarrow hcp}$  and  $\Delta G_{Mag}^{fcc \rightarrow hcp}$ . The Néel transition of most high-Mn TWIP and TRIP steels (especially those with Al and Si additions) is slightly below room temperature [57], save for the Fe-22Mn-0.6C wt.% grade [4]. Interestingly, stabilization of the FCC phase due to antiferromagnetic effects still occurs, owing to the gradual nature of this transition [4,57,58,76].

#### 4.4 Interfacial Energy Calculation and Behavior

In each alloy the interfacial energy is the major component of the SFE. The term  $\sigma^{\gamma/\epsilon}$  is  $9.2 \pm 1.6$ ,  $8.6 \pm 1.7$  and  $11.8 \pm 2.7$  mJ m<sup>-2</sup> for the Fe-22/25/28Mn-3Al-3Si alloys, respectively, from Equation (4). The uncertainty of  $\sigma^{\gamma/\epsilon}$  is obtained from the root sum square of the uncertainties of  $\gamma_{exp}$  and  $2\rho E_{str}$  then dividing this quantity by two. Using the same methodology, interfacial energy values were calculated for binary Fe-16/18/20/25Mn, Fe-18Mn-0.6-0/1.5Al and Fe-18Mn-0.6C-0/1.5Si alloys from existing data in the literature. The calculation of  $\sigma^{\gamma/\epsilon}$  used values of  $\gamma_{exp}$  reported by Volosevich et al. [31] (Fe-16/18/20/25Mn), Kim et al. [10] (Fe-18Mn-0.6-0/1.5Al) and Jeong et al. [11] (Fe-18Mn-0.6C-0/1.5Si). Values of  $E_{str}$  were calculated using lattice parameters in references [52] and [53] and the procedure outlined in section 4.2. Lattice parameters of the FCC and HCP phase of the Fe-18Mn-0.6C-0/1.5(Al/Si)

alloys were assumed to be equal to the binary Fe-18Mn alloy for the purpose of calculating  $E_{str}$ . The shear modulus and Poisson ratio used in the calculation of  $E_{str}$  are provided in Table 3. The values of  $2\rho(\Delta G_{chem}^{fcc \rightarrow hcp} + \Delta G_{Mag}^{fcc \rightarrow hcp})$  were determined with the thermodynamic model developed in section 4.3. A summary of some of the parameters used in the calculation of  $\sigma^{\gamma/\epsilon}$  are listed in Table 3. The interfacial energies of the Fe-18Mn-0.6C-0/1.5(Al/Si) range from 8.6 to 11.5 mJ m<sup>-2</sup> and are consistent with a range of 8.6 to 11.8 mJ m<sup>-2</sup> for the Fe-22/25/28Mn-3Al-3Si alloys. Interstitial C segregation may influence the experimental SFE measurements but is not accounted for in  $\Delta G_{chem}^{fcc \rightarrow hcp}$  and  $\Delta G_{Mag}^{fcc \rightarrow hcp}$  (due to the assumption of homogenous compositions). Therefore, Mosecker and Saeed-Akbari [12] proposed that the effects of interstitial segregation on  $\gamma_{exp}$  would be accounted for in the calculation of  $\sigma^{\gamma/\epsilon}$ . However, no substantial differences in the calculated values of  $\sigma^{\gamma/\epsilon}$  are observed between the Fe-22/25/28Mn-3Al-3Si and Fe-18Mn-0.6C-0/1.5(Al/Si) alloys, suggesting the influence of segregation on the SFE measurements is minor. The calculated interfacial energies of the binary Fe-16/18/20//22/25Mn wt.% alloys range from 15.7 to 32.5 mJ m<sup>-2</sup> and are higher than for the other alloys. A comparison of the interfacial energies of Fe-22/25Mn and Fe-22/25Mn-3Al-3Si indicates an offset of  $\sim 3$  mJ m<sup>-2</sup>. One explanation for the offset is that values of  $\gamma_{exp}$  [31] used in the interfacial calculation are higher than the actual values (as previously discussed) and therefore result in an overestimate of the interfacial energies for the binary Fe-Mn alloys. However, the trend in  $\gamma_{exp}$  vs. Mn reported by Volosevich et al. [31] is similar to other works [26,76] and provides confidence that the general trend in  $\sigma^{\gamma/\epsilon}$  (which is calculated from  $\gamma_{exp}$ ) with changes in Mn content reflects the actual behavior.

In Figure 9, the values of  $\sigma^{\gamma/\varepsilon}$  are plotted as a function of  $2\rho(\Delta G_{chem}^{fcc\rightarrow hcp} + \Delta G_{Mag}^{fcc\rightarrow hcp})$  for all alloys. The dependence of  $\sigma^{\gamma/\varepsilon}$  on  $2\rho(\Delta G_{chem}^{fcc\rightarrow hcp} + \Delta G_{Mag}^{fcc\rightarrow hcp})$  is consistent with parabolic behavior. In general, as  $|2\rho(\Delta G_{chem}^{fcc\rightarrow hcp} + \Delta G_{Mag}^{fcc\rightarrow hcp})|$  increases, the term  $\sigma^{\gamma/\varepsilon}$  also increases, indicating the interfacial energy is strongly related to  $|\Delta G_{Chem}^{fcc\rightarrow hcp} + \Delta G_{Mag}^{fcc\rightarrow hcp}|$ . Conversely, as  $|\Delta G_{Chem}^{fcc\rightarrow hcp} + \Delta G_{Mag}^{fcc\rightarrow hcp}|$  approaches 0, where both FCC and HCP phases are equally favored, the resulting energy increase at the interface should be near a minimum, as is observed. Therefore,  $\sigma^{\gamma/\varepsilon}$  can be approximated as a parabolic function of  $2\rho(\Delta G_{Chem}^{fcc\rightarrow hcp} + \Delta G_{Mag}^{fcc\rightarrow hcp})$  with a minimum at  $\sigma_{min}^{\gamma/\varepsilon}$ :

$$\sigma^{\gamma/\varepsilon} = c(2\rho(\Delta G_{Chem}^{fcc\rightarrow hcp} + \Delta G_{Mag}^{fcc\rightarrow hcp}))^2 + \sigma_{min}^{\gamma/\varepsilon} \quad (\text{mJ m}^{-2}) \quad (29)$$

where  $c$  is a constant determined from fitting to experimental values. The term  $\sigma_{min}^{\gamma/\varepsilon}$  is  $9.5 \text{ mJ m}^{-2}$  and results from the minimum fit for the Fe-22/25/28Mn-3Al-3Si and Fe-18Mn-0.6C-0/1.5(Al/Si) alloys. The constant ‘‘c’’ of 0.01 was determined by fitting a curve (dotted line in Figure 9) to the trend in  $\sigma^{\gamma/\varepsilon}$  as a function of  $2\rho(\Delta G_{Chem}^{fcc\rightarrow hcp} + \Delta G_{Mag}^{fcc\rightarrow hcp})$  for the Fe-Mn-Al-Si, Fe-Mn-Al-C and Fe-Mn alloys.

Non-monotonic behavior of  $\sigma^{\gamma/\varepsilon}$  as a function of composition has been reported by other authors. Cotes et al. [30] showed that  $\sigma^{\gamma/\varepsilon}$  varies as a function of Mn content for binary Fe-Mn alloys and can be approximated as an upward opening parabolic curve, with a minimum  $\sigma^{\gamma/\varepsilon}$  occurring between 20 and 25 wt.% Mn. Mosecker et al. [12] reported a similar behavior for the Fe-Mn-Cr-N system, where  $\sigma^{\gamma/\varepsilon}$  displays parabolic behavior with additions of nitrogen from 0.2 to 0.9 wt.%. These studies provides additional confidence that the underlying cause of the

parabolic behavior is due to the relationship between  $\sigma^{\gamma/\varepsilon}$  and  $|\Delta G_{Chem}^{fcc \rightarrow hcp} + \Delta G_{Mag}^{fcc \rightarrow hcp}|$  as proposed in the present work.

#### 4.4 Model Validation

The thermodynamic model and the empirical relationship for  $\sigma^{\gamma/\varepsilon}$  were used in conjunction to predict values of  $\gamma_{exp}$  and compare them with values from the literature. The calculated values of  $\gamma_{exp}$  (note: the calculated value includes  $2\rho E_{str}$ ) are 16.7 and 28.9 mJ m<sup>-2</sup> for Fe-18Mn-0.6C-0/1.5Al alloys and exhibit good agreement with experimental values of 13±3/30±10 mJ m<sup>-2</sup> [10] and 19.3±2.5/29.1±2.5 mJ m<sup>-2</sup>, respectively. Jung and De Cooman [78] reported mechanical twinning in an Fe-18Mn-0.6C-2.5Al alloy. The calculated values of  $\gamma_{exp}$  and  $\gamma_{\infty}$  for this alloy are 40.4 and 34.8 mJ m<sup>-2</sup> which is in the SFE range for mechanical twinning as reported by Allain et al. [24]. The calculated SFE values are reasonable for C contents up to 0.6 wt.%. In addition, the present SFE measurements for the Fe-22/25/28Mn-3Al-3Si alloys give confidence that the model is valid for Al additions up to 3 wt.%.

The range of Si for which the model is valid was tested by predicting T<sub>0</sub> temperatures (in this work the T<sub>0</sub> temperature is defined as the average of the  $\varepsilon$ -martensite start (Ms) and austenite start (As) temperatures and corresponds to  $(\Delta G_{Chem}^{fcc \rightarrow hcp} + \Delta G_{Mag}^{fcc \rightarrow hcp}) = 0$ ) of ternary Fe-Mn-Si alloys and comparing them to experimental values reported by Cotes et al.[71,79]. The results of this comparison are reported in Table 5. Analysis of the data indicates that good agreement is achieved between the experimental and calculated T<sub>0</sub> temperatures (within 7%) for Si additions up to ~6 wt.% in ternary Fe-Mn-Si alloys. At high Mn contents (28-29 wt.%), a greater deviation (~11-13%) is observed in the predicted vs. experimental T<sub>0</sub> temperatures. Therefore, the model is valid for a range of Mn content from 16 to 29 wt.% [29]. Jeong et al. [11] reported SFE measurements of 19.8 ±2.5 and 13.8 ±2.5 mJ m<sup>-2</sup> for paramagnetic Fe-18Mn-0.6C and Fe-

18Mn-0.6C-1.5Si wt.% alloys, respectively, finding that additions of Si resulted in a decrease of 3.5 mJ m<sup>-2</sup> per wt.%. The current thermodynamic model predicts values of  $\gamma_{exp}$  of 17.0 and 15.4 mJ m<sup>-2</sup> for the same alloys, corresponding to a decrease in  $\gamma_{exp}$  of ~1 mJ m<sup>-2</sup> per wt.% addition of Si. Tian and Zhang [61] experimentally measured a decrease  $\gamma_{exp}$  of ~2.5 mJ m<sup>-2</sup> per wt.% addition of Si in Fe-32Mn-0/4.6Si-0.2C alloys [61]. While the model improves upon previous thermodynamic models which report an increase in SFE for small additions of Si, the present thermodynamic model would likely benefit from interaction parameters for Fe-Si-C for the HCP phase, an observation also shared by Jeong et al. [11]. Therefore, the model should be limited to Si concentrations of up to 1.5 wt.% for alloys with C contents of ~0.6 wt.%.

The values of  $2\rho\Delta G_{Mag}^{fcc\rightarrow hcp}$ ,  $2\rho\Delta G_{Chem}^{fcc\rightarrow hcp}$ ,  $2\rho E_{str}$  and  $\sigma^{\gamma/\varepsilon}$  determined in this work (Figure 8) provide a greater understanding of the physical phenomena behind the SFE evolution in Fe-Mn based steels. Of particular interest is the interfacial energy parameter, which is typically the largest parameter to contribute to the SFE in these materials at RT. This parameter exhibits a minimum near the point at which the Gibbs free energies of FCC and HCP phases are equal and increases when the absolute value of the term  $2\rho(\Delta G_{Chem}^{fcc\rightarrow hcp} + \Delta G_{Mag}^{fcc\rightarrow hcp})$  becomes larger (see Figure 9). In the present Fe-22/25/28Mn-3Al-3Si steels, for additions of Mn above ~23.5 wt.%, the terms  $\sigma^{\gamma/\varepsilon}$ ,  $2\rho\Delta G_{Mag}^{fcc\rightarrow hcp}$  and  $2\rho\Delta G_{Chem}^{fcc\rightarrow hcp}$  all make positive contributions, resulting in a sharp rise of the SFE. However, when decreasing the Mn content from ~23.5 wt.%, only the interfacial energy increases and makes a positive contribution to the SFE. This results in a much flatter SFE curve in this region or a minimum, observed in both experimental [31,32] and theoretical studies [26,29], before a subsequent increase in SFE occurs with further reductions in Mn content.

## 5. Summary and Conclusions

In this study the effect of Mn content on the SFE was investigated by measuring dissociation widths of partial-dislocation pairs in three alloys (Fe-22/25/28Mn-3Al-3Si wt.%) using TEM. The experimental SFE values of  $15 \pm 3$ ,  $21 \pm 3$  and  $39 \pm 5$   $\text{mJ m}^{-2}$  exhibit a super-linear increase in SFE from 22 to 28 wt.% Mn. The strain energy associated with the contraction in molar volume during the austenite to  $\epsilon_{\text{hcp}}$ -martensite transformations was determined to be  $\sim 1-4$   $\text{mJ m}^{-2}$ , yielding ideal SFE values of  $14 \pm 3$ ,  $20 \pm 3$  and  $37 \pm 5$   $\text{mJ m}^{-2}$ .

A new thermodynamic model for the Fe-Mn-Al-Si-C system is proposed which determines the chemical and magnetic components of the difference in Gibbs free energy of the FCC and HCP phases. The ideal SFE values were used in conjunction with the thermodynamic phase data to determine the FCC/HCP interfacial energies of the three Fe-Mn-(Al-Si) steels as well as Fe-Mn and Fe-Mn-C-Al/Si alloys for which experimental SFE data is available in the literature. Calculations of the FCC/HCP interfacial energy parameter yielded values ranging from 8.6 to 11.8  $\text{mJ m}^{-2}$  for the Fe-22/25/28Mn-3Al-3Si and Fe-18Mn-0.6C-0/1.5(Al/Si) wt.% TRIP and TWIP alloys. The interfacial energy of the binary Fe-Mn alloys ranged from 15.7 to 32.5  $\text{mJ m}^{-2}$ . The present work shows a strong correlation between the value of the interfacial energy of Fe-Mn-(Al, Si, C) steels and the difference in free energy of the FCC and HCP phases. To improve the accuracy of SFE calculations, an empirical relationship to describe the interfacial energy is proposed for use in SFE calculations. The combined thermodynamic model and empirical relationship exhibit good agreement with the present SFE measurements, and those in the literature, making it a useful tool for the design of high-Mn TRIP/TWIP steels. A follow on

study will investigate the relationship between SFE value, microstructural evolution and mechanical properties.

This work is sponsored by the National Science Foundation Division of Materials Research, USA, under grant DMR0805295 and by the Comisión Interministerial de Ciencia y Tecnología (CICYT), Spain, under Grant MAT2012-39124. We would like to thank Dr. Bengt Hallstedt, Materials Chemistry, RWTH Aachen University, for the technical discussions.

### References

1. Grässel O, Krüger L, Frommeyer G, Meyer LW. *Int J Plast* 2000;16:1391.
2. Barbier D, Gey N, Allain S, Bozzolo N, Humbert M. *Mat Sci Eng A* 2009; 500:196.
3. Curtze S, Kuokkala VT. *Acta Mater.* 2010;58:5129.
4. Bouaziz O, Allain S, Scott CP, Cugy P, Barbier D. *Curr Opin Solid State Mater Sci* 2011;15:141.
5. Vercammen S. *Processing and Tensile Behaviour of TWIP Steels, Microstructural and Textural Analysis.* Leuven: Katholieke Universiteit Leuven; 2004.
6. De Cooman BC, Kwon O, Chin KG. *J Mater Sci Technol* 2012;28:513.
7. Saeed-Akbari A, Mosecker L, Schwedt A, Bleck W. *Metall Mater Trans A* 2012;43:1688.
8. Saeed-Akbari A, Schwedt A, Bleck W. *Scripta Mater* 2012;66:1024.
9. Gutierrez-Urrutia I, Raabe D, *Acta Mater* 2011;59:6449
10. Kim J, Lee SJ, De Cooman BC. *Scripta Mater* 2011;65:363.
11. Jeong K, Jin JE, Jung YS, Kang S, Lee YK. *Acta Mater* 2013;61:3399.
12. Mosecker L, Saeed-Akbari A. *Sci Technol Adv Mater* 2013;14:1.
13. Gutierrez-Urrutia I, Raabe D. *Acta Mater* 2012;60:5791.
14. Steinmetz DR, Jäpel T, Wietbrock B, Eisenlohr P, Gutierrez-Urrutia I, Saeed-Akbari A, Hickel T, Roters F, Raabe D. *Acta Mater* 2013;61:494.
15. Gutierrez-Urrutia I, Zaefferer S, Raabe D. *Mat Sci Eng A* 2010;527:3552.
16. Remy L. *Acta Metall* 1978;26:443
17. Bouaziz O, Guelton. *Mat Sci Eng A* 2001;319-321:246
18. Allain S, Chateau J-P, Bouaziz O. *Mat Sci Eng A* 2004;387-389:143

19. Bouaziz O, Allain S, Scott C. *Scripta Mater* 2008;58:484
20. Barbier D, Favier V, Bolle B. *Mat Sci Eng A* 2012;540:212
21. Dancette S, Delannay L, Renard K, Melchior MA, Jacques PJ. *Acta Mater* 2012;60:2135
22. Kim J, Estrin Y, Beladi H, Timokhina I, Chin KG, Kim SK, De Cooman BC. *Metall Mater Trans* 2012;43:479.
23. Grässel O, Frommeyer G, Derder C, Hofmann H. *J Physique IV* 7 1997;C5:383.
24. Allain S, Chateau JP, Bouaziz O, Migot S, Guelton N. *Mat Sci Eng A* 2004;387-389:158.
25. Dumay A, Chateau JP, Allain S, Migot S, Bouaziz O. *Mat Sci Eng A* 2008;483-484:184.
26. Saeed-Akbari A, Imlau J, Prael U, Bleck W. *Metall Mater Trans A* 2009;40:3076.
27. Wittig JE, Pozuelo M, Jimenez JA, Frommeyer G. *Steel Res Int* 2009;80:66.
28. Olson GB, Cohen M. *Metall Trans A* 1976;78:1897.
29. Nakano J, Jacques PJ. *CALPHAD* 2010;34:167.
30. Cotes SM, Fernandez Guillermet A, Sade M. *Metall Mater Trans A* 2004;35:83.
31. Volosevich PY, Gridnev VN, Petrov YN. *Phys Met Metallogr* 1976;42:126.
32. Volosevich PY, Gridnev VN, Petrov YN. *Phys Met Metallogr* 1975;40:90.
33. Bampton CC, Jones IP, Loretto MH. *Acta Metal* 1978;26:39.
34. Pierce DT, Bentley J, Jimenez JA, Wittig JE. *Scripta Mater* 2012;66:753.
35. Idrissi H, Renard K, Ryelandt L, Schryvers D, Jacques PJ. *Acta Mater* 2010;58:2464.
36. Hirth JP, Lothe J, *Theory of Dislocations*, 2nd ed. New York: Wiley; 1982.
37. Gebhardt T, Music D, Kossmann D, Ekholm M, Abrikosov IA, Vitos L, Schneider JM. *Acta Mater* 2011;59:3145.
38. Reeh S, Music D, Gebhardt T, Kasprzak M, Jäpel T, Zaefferer, Raabe D, Richter S, Schwedt A, Mayer J, Wietbrock B, Hirt G, Schneider JM. *Acta Mater* 2012;60:6025.
39. Friak M, Hickel T, Körmann F, Udyansky A, Dick A, Von Pezold J, Ma D, Kim O, Counts WA, Sob M, Gebhardt T, Music D, Schneider J, Raabe D, Neugebauer J. *Steel Research Int* 2011;82:86.
40. Pierce DT, Nowag K, Montagne A, Jiménez JA, Wittig JE, Ghisleni R. *Mat Sci Eng A* 2013;578:134.
41. Cockayne DJH. *Z Naturforsch* 1972;27a:452.
42. Cockayne DJH. *J Physique* 1974;35:141.

43. Williams DB, Carter CB, Transmission Electron Microscopy, a Text Book for Materials Science, 2nd ed. New York: Springer; 2009.
44. Edington JW. Practical Electron Microscopy in Materials Science. Herndon: Tech Books;1976
45. Aerts E, Delavignette P, Siems R, Amelinckx S. J Appl Phys 1962;33:3078.
46. Teutonico LJ. Philos Mag 1966;15:959.
47. Eshelby JD, Read WT, Shockley W. Acta Metal 1953;1:251.
48. Foreman AJE. Acta Metal 1955;3:322.
49. Teutonico LJ. Acta Metal 1963;11:1283.
50. Cockayne DJH, Vitek V. Phys Stat Sol B 1974;65:751.
51. Brooks JW, Lorreto MH, Smallman RE. Acta Metal 1979;27:1839.
52. Marinelli P, Baruj A, Fernandez Guillermet A, Sade M. Z Metallkd 2001;91:957.
53. Marinelli P, Baruj A, Fernandez Guillermet A, Sade M. Z Metallkd 2001;92:489.
54. Müllner P, Ferreira PJ. Philos Mag Lett 1996;73:289.
- 55 Eshelby JD. Proc Roy Soc A 1957;241:376
- 56 Jin JE, Jung M, Lee CY, Jeong J, Lee YK. Met Mater Int 2012;18:419
- 57 Jung I, Lee S-J, De Cooman B-C. Scripta Mater 2012;66:729
- 58 King HW, Peters MA. Can Met Q 1997;36:137
- 59 Huang W. CALPHAD 1989;13:243
- 60 Tian X, Zhang Y. Mat Sci Eng A 2009;516:78
- 61 Tian X, Zhang Y. Mat Sci Eng A 2009;516:73
- 62 Djurovic D, Hallstedt B, Von Appen J, Dronskowski R. CALPHAD 2010;34:279
- 63 Djurovic D, Hallstedt B, Von Appen J, Dronskowski R. CALPHAD 2011;35:479
- 64 Frisk K. CALPHAD 1993;17:335
65. Dinsdale AT. CALPHAD 1991;15:317.
- 66 Gustafson P. Scand J Metall 1985;14:259
- 67 Shukla A, Pelton AD. J Phase Equilib Diffus 2009;30:28
- 68 LaCaze J, Sundman B. Metall Trans A 1991;22:2211
- 69 Miettinen J. CALPHAD 1998;22:231.

70. Li L, Hsu TY, Calphad 1997;21:443.
- 71 Cotes S, Fernandez Guillermet A, Sade M. J Alloys Compd 1998;280:168
- 72 Forsberg A, Agren J. J Phase Equilib 1993;14:354
- 73 Yang WS, Wan CM. J Mater Sci 1990;25:1821.
- 74 Hillert M, Jarl M. CALPHAD 1978;2:227.
- 75 Inden G. Phys B 1981;103:82.
- 76 Cankurtaran M, Saunders GA, Ray P, Wang Q. Phys Rev B 1993;47:3161
- 77 Schumann H. Kristall und Technik 1974;9:1141
- 78 Jung I-C, De Cooman B-C. Acta Mat 2013;61:6724
- 79 Cotes S, Fernandez Guillermet A, Sade M. J Alloys Compd 1998;278:231

### Figure Captions

Figure 1 – Images of dislocations in 22%Mn specimens deformed to the YP. (a) WBDF and (b) corresponding BF image of a partial-dislocation pair. (c) WBDF image of a second partial dislocation pair closer to screw character and displaying reduced separation. Only a few representative separation measurements are shown.

Figure 2 – WBDF images of partial-dislocation pairs in a 22%Mn alloy deformed to the YP. In (a) the partials display non-uniform separation, most dramatically at the intersections with the foil surfaces. In (b) a partial-dislocation pair residing in (111) normal to the [111] beam direction is interacting with a stacking fault on (-111). In (c), the defects in (b) are imaged with a 02-2 diffracting vector leading to invisibility of one of the partials in (111) and the SF on (-111).

Figure 3 – A WBDF image of a partial-dislocation pair in an Fe-25Mn-3Al-3Si alloy deformed to the YP.

Figure 4 – WBDF images of partial-dislocation pairs in specimens of the 28%Mn alloy deformed to (a) the YP and (b) 1.5% with heat treatment of 650°C for 48 h.

Figure 5 – Dark-field images of intrinsic SFs in (a) the 22%Mn, (b) the 25%Mn and (c) the 28%Mn alloys as identified by the procedure in [43,44].

Figure 6 – Average actual partial-dislocation separations for the 22, 25 and 28%Mn alloys for specimens deformed to the YP and 1.5% with heat treatments. The error bars represent the standard deviation of the measurements on individual pairs. The dashed and solid curves represent theoretical partial-dislocation spacings based on isotropic and anisotropic elasticity, respectively. The dash dot line for the 28%Mn alloy assumes a Peierls core model. The larger symbols correspond to the partial dislocations from Figures 1, 3 and 4.

Figure 7 – XRD patterns for (top) an Fe-22Mn-3Al-3Si alloy deformed at room temperature, (middle) an Fe-25Mn-3Al-3Si alloy deformed at -25°C and (bottom) an Fe-28Mn-3Al-3Si alloy deformed at -100°C. All samples deformed to maximum uniform elongation. The peaks are labeled according to phase and reflection in miller indices.

Figure 8 – Experimental effective SFE ( $\gamma_{exp}$ ) and ideal SFE ( $\gamma_{\infty}$ ) values with error bars representing the standard deviation of the measurements. Chemical ( $n\rho\Delta G_{Chem}^{fcc\rightarrow hcp}$ ) and magnetic ( $n\rho\Delta G_{Mag}^{fcc\rightarrow hcp}$ ) contributions to the difference in Gibbs free energy from the FCC to HCP phase transformation determined by thermodynamic model (note: the values of  $n\rho\Delta G_{Chem}^{fcc\rightarrow hcp}$  denoted by the dashed line were calculated using  $L_{Fe,Mn:Va}^{HCP}$  proposed by Djurovic et al. [63]). Interfacial parameters  $\sigma^{\gamma/\epsilon}$  calculated from the experimental and theoretical data. All values are plotted as a function of Mn content. The dash-dot line indicates Mn content at which the Néel transition occurs at 298K for an Fe-XMn-2.7Al-2.9Si wt.% steel [58].

Figure 9 – Interfacial energy plotted as a function of  $2\rho(\Delta G_{Chem}^{fcc\rightarrow hcp} + \Delta G_{Mag}^{fcc\rightarrow hcp})$  for Fe-22/25/28Mn-3Al-3Si, Fe-16/18/20/22/25Mn and Fe-18Mn-0.6C-0/1.5(Al/Si) wt.% steels. The dashed line represents the fit of the calculated interfacial energies.

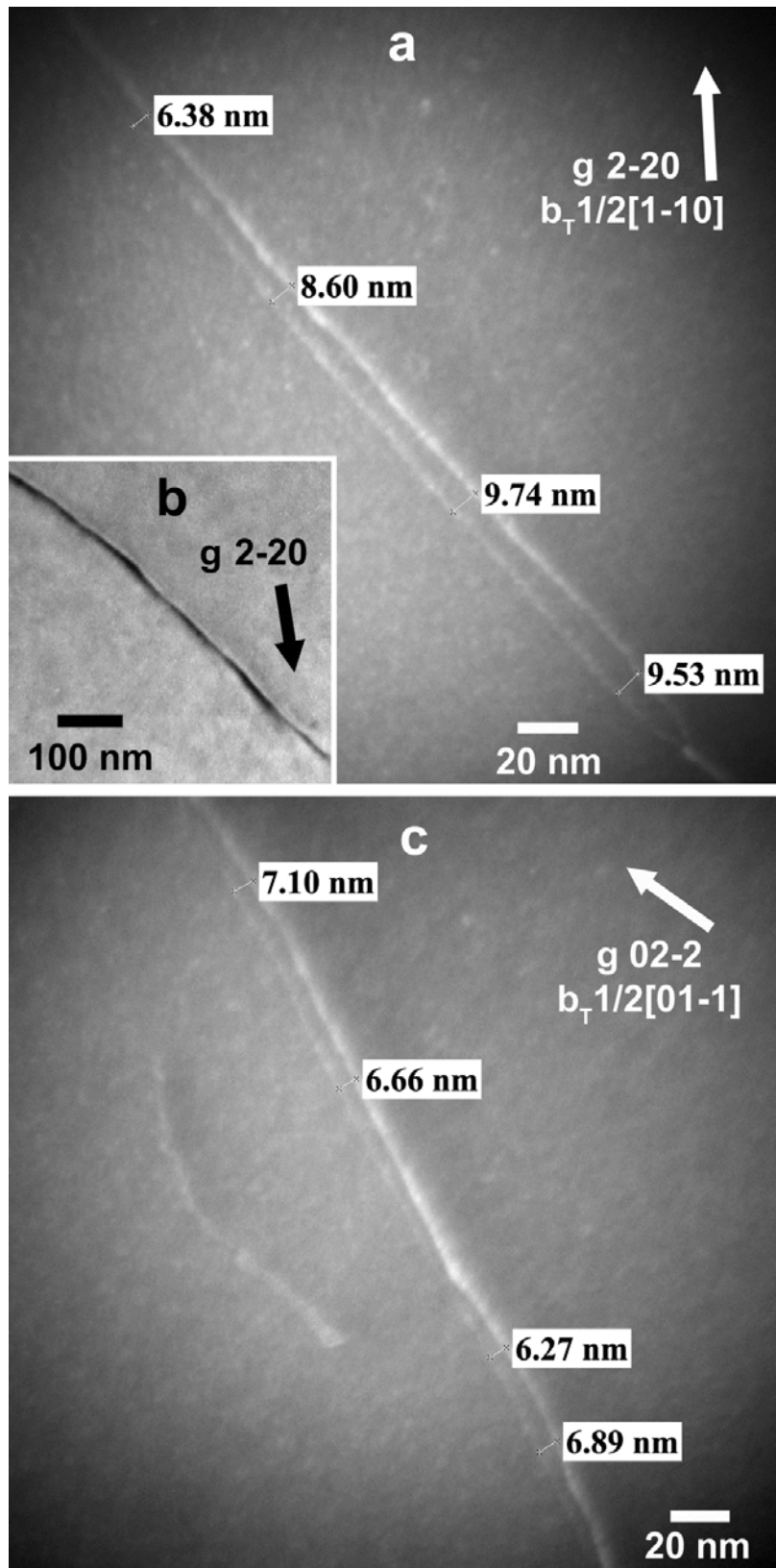


Figure 1

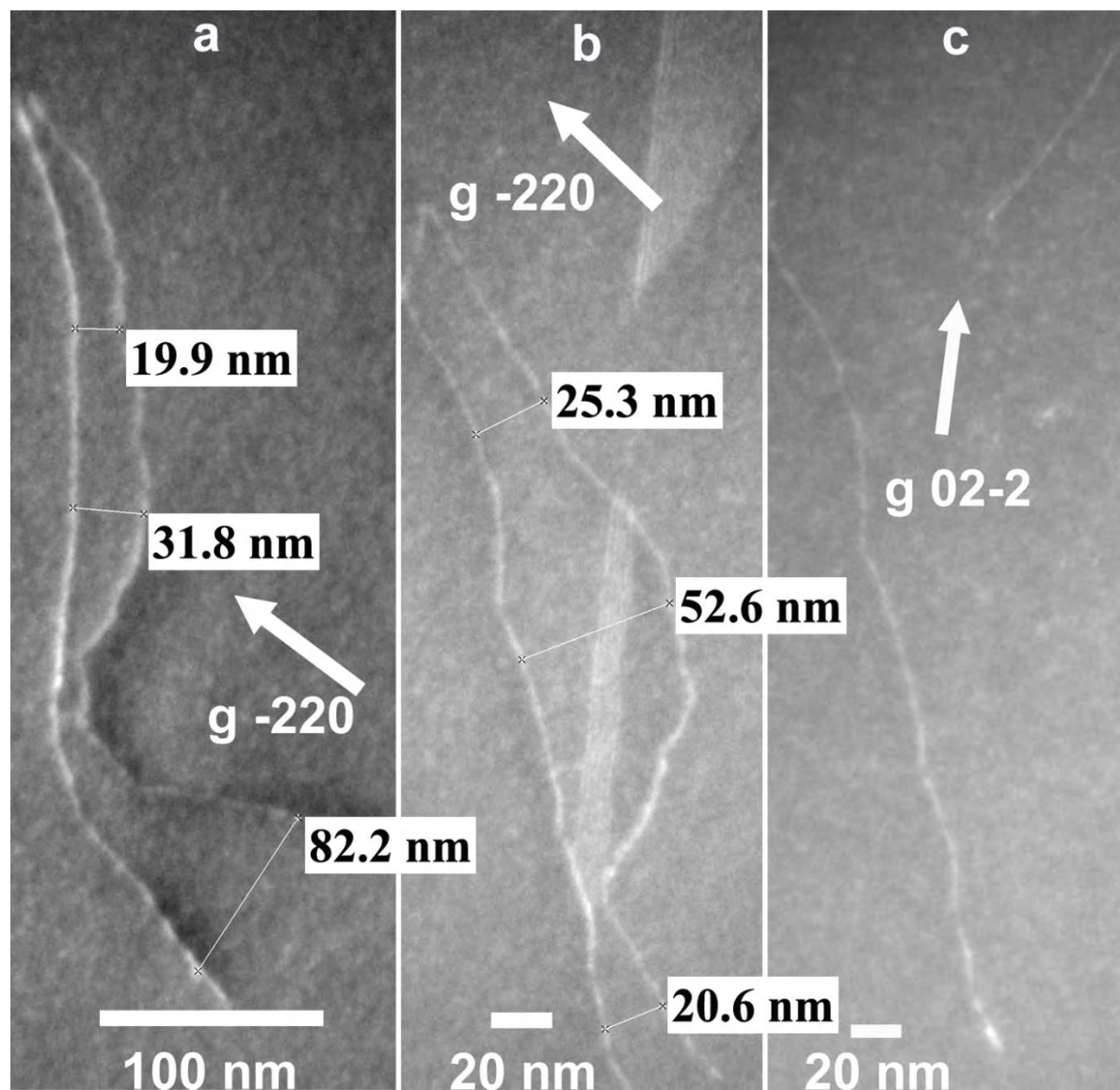


Figure 2

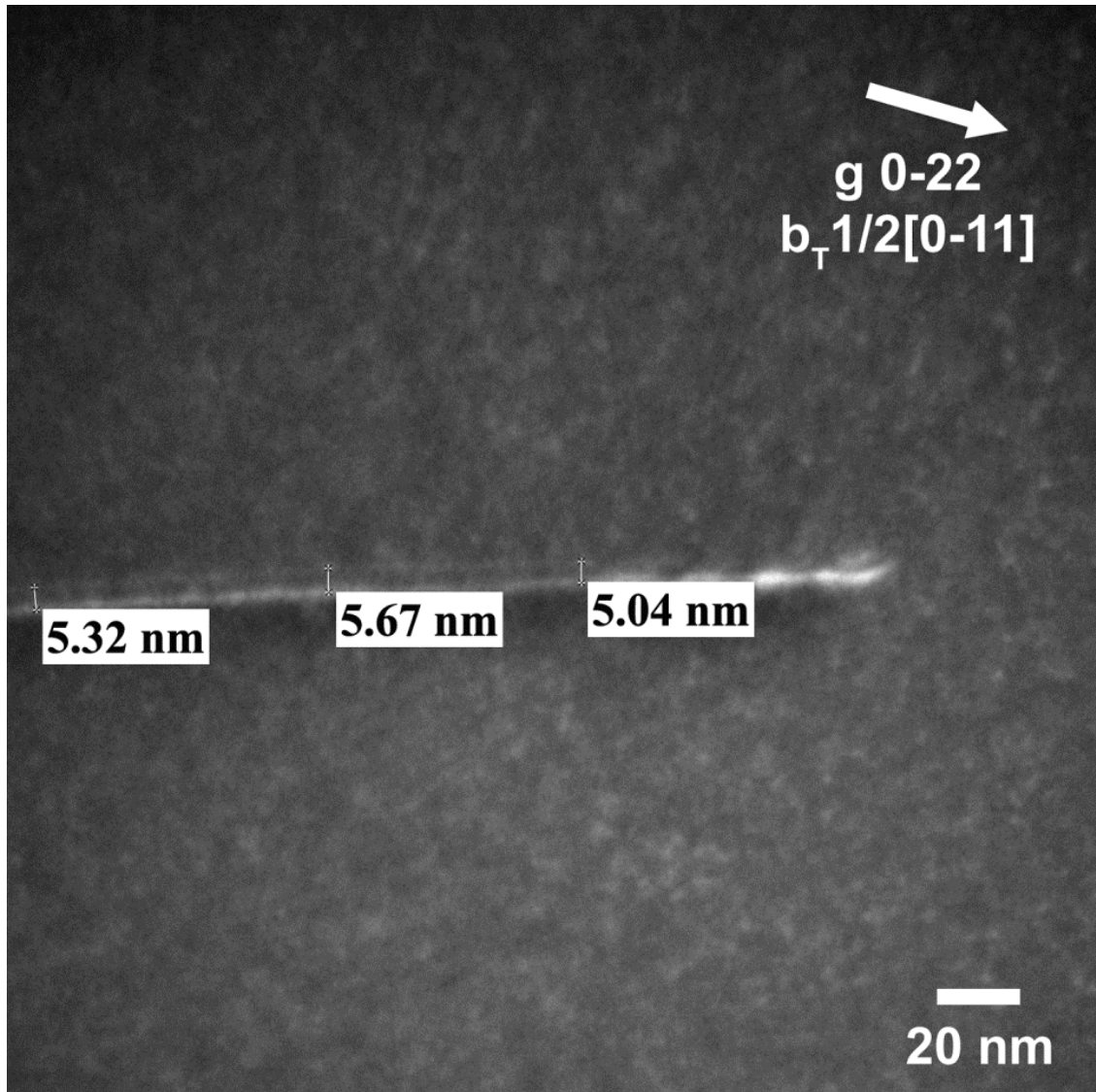


Figure 3

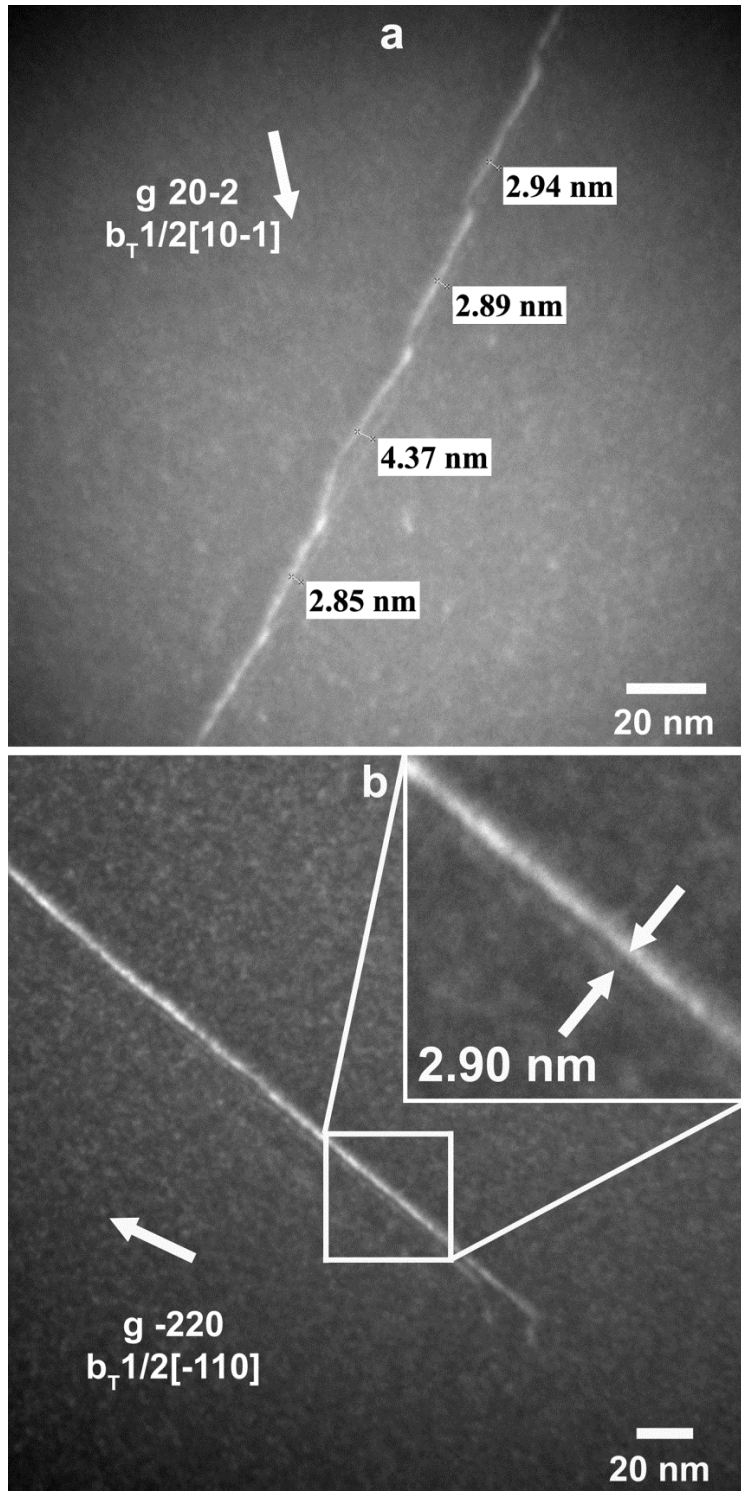
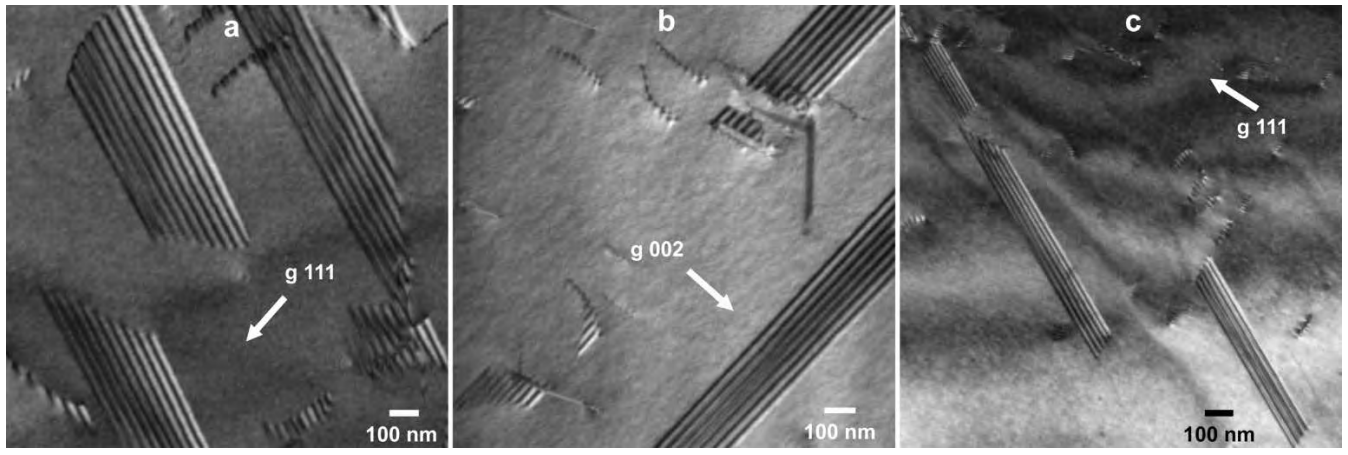


Figure 4



**Figure 5**

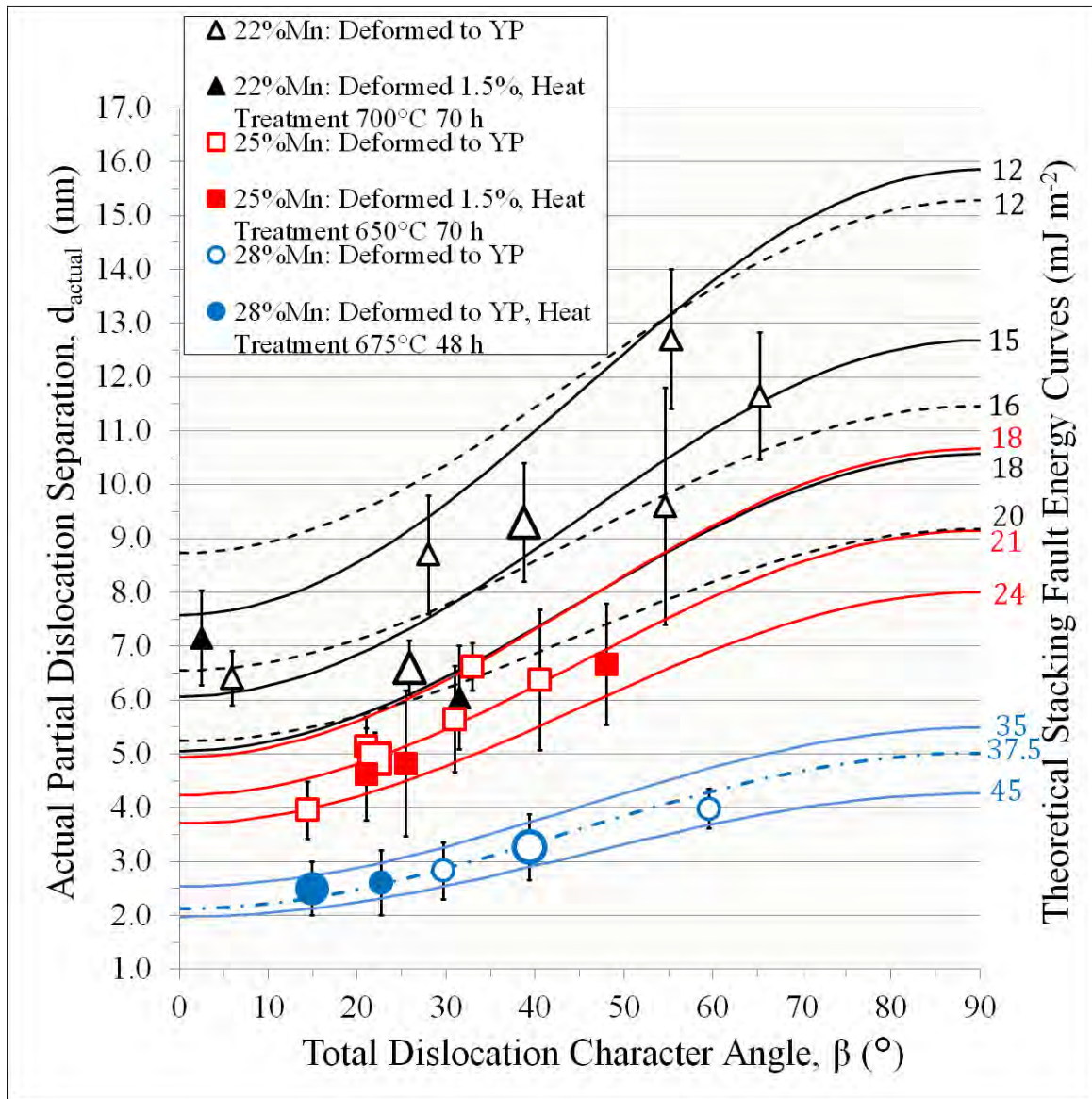


Figure 6

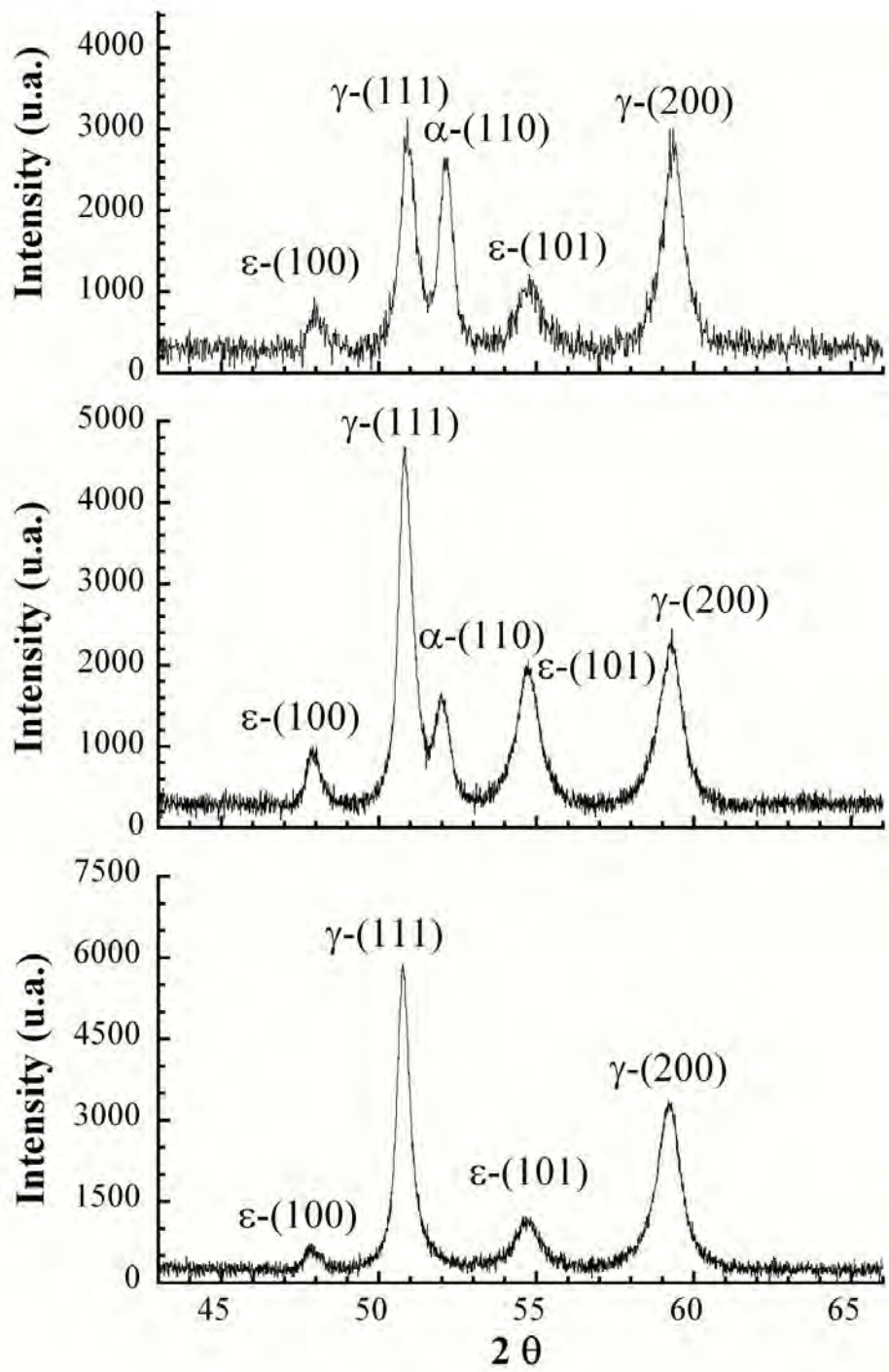


Figure 7

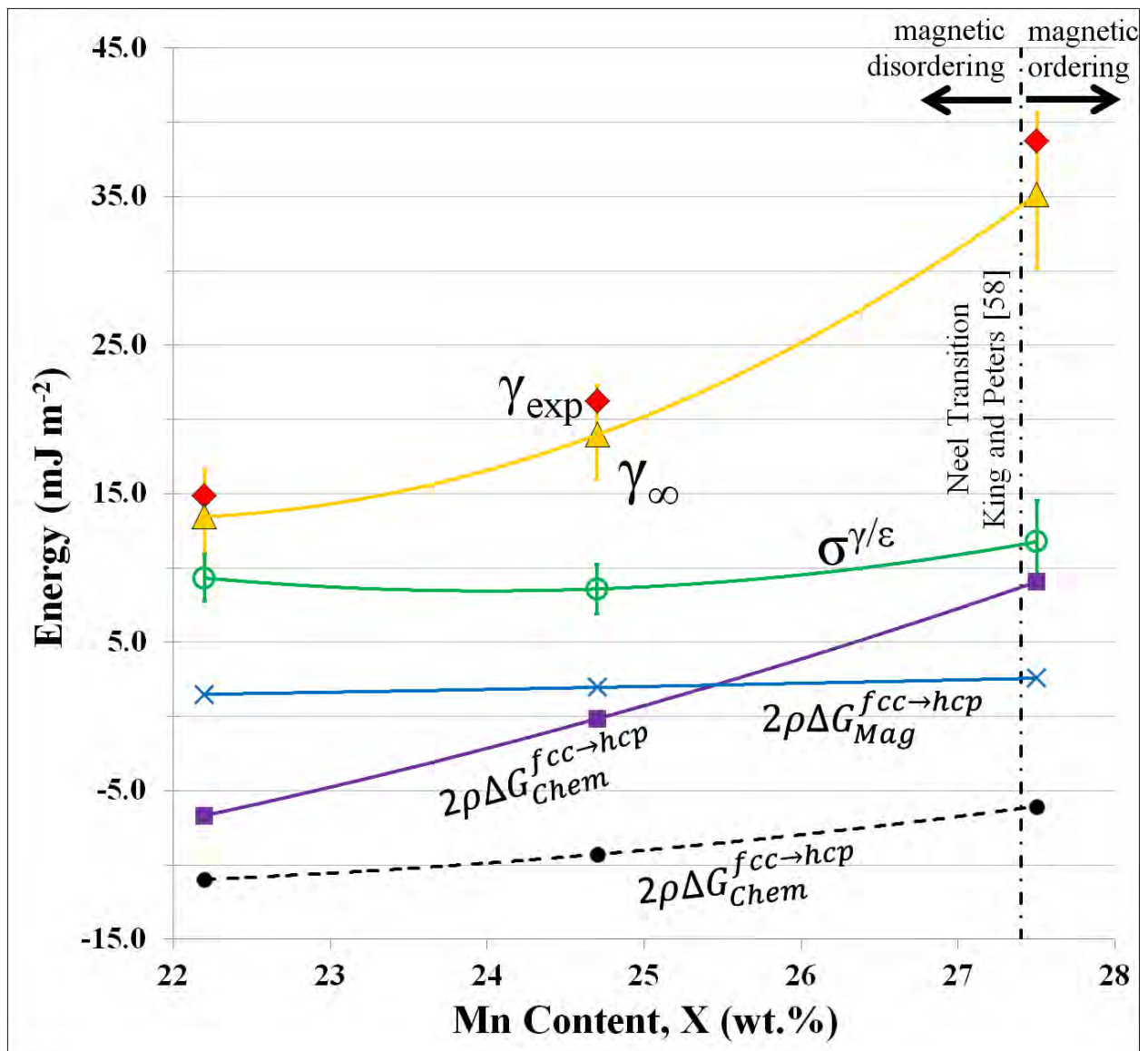


Figure 8

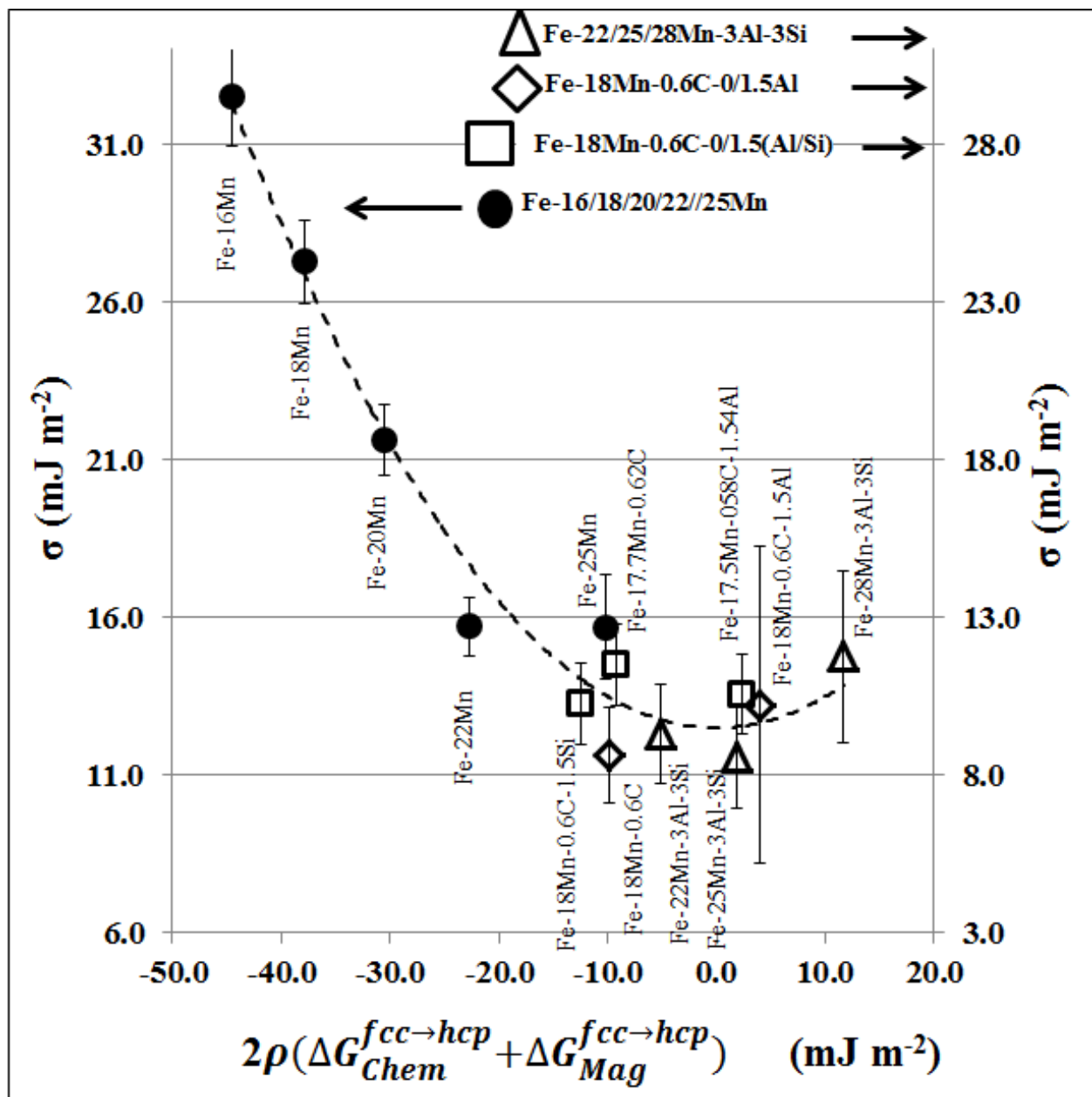


Figure 9